Synergistic effect of surfactants in porous geopolymer: Tailoring pore size and pore connectivity

K.M. Klima [a], C.H. Koh [a], H.J.H. Brouwers [a], Qingliang Yu [a,b,*]

[a] *Department of the Built Environment, Eindhoven University of Technology, Eindhoven, 5600 MB, the Netherlands*
[b] *School of Civil Engineering, Wuhan University, Wuhan, 430072, PR China*

ABSTRACT

With the growing interest in foamed geopolymer manufacture, there is an increasing demand for tailoring these composites' pore structure. The binary system of two surfactants offers a possibility for enhancing foam formation efficiency and stability in geopolymer paste, however, their effects are not well understood. The influence of binary system blends on pore formation, size, and distribution in fly ash-based geopolymer matrix is investigated and their synergistic effects are evaluated. The results show that combining a nonionic surfactant with anionic Sodium Dodecyl Sulfate (SDS) increases open porosity, whereas cationic Cetyltrimethylammonium Bromide (CTAB) promotes the development of closed pores, improving thermal insulating, hygrothermal and mechanical performance. Moreover, this paper proposes a mechanism to describe the creation of pores in the presence of mixed micelles, as well as the benefit of employing mixed surfactant systems in customizing porous composites.

1. Introduction

There is a growing interest in the development of geopolymer, in a specific direction of fireproof and thermal insulations. It can be stated that geopolymer is an attractive alternative for a range of thermo-acoustic insulating and fire-proofing applications as its chemical and mineralogical composition contributes to fundamentally excellent thermal performance [1]. Moreover, these characteristics can be further enhanced by finetuning the porosity and pore structure by means of for instance introducing air into the matrix. However, research on this topic is still rather limited and lacks sufficient consensus.

Porosity is a significant parameter to provide material characterized by low density and low thermal conductivity which are crucial for designing, for instance, protective materials for high-temperature applications. However, the distribution of pore size and the character of pores, i.e. the proportion of open pores, establish a material's suitability for particular applications. For fire-resistant composites exposed to high temperatures, it is advantageous to have an open pore structure that facilitates the transport of water vapour through the material, which significantly minimizes the risk of moisture clog, cracks formation, propagation and spalling [2]. Materials for thermal insulation applications have different requirements regarding the pore structure. The

pores are desirably closed because increasing the open porosity increases gas permeability, including air, which is a heat transfer medium. Porous sound absorbents, as indicated by Cao et al. [3], should consist of a significant number of pores (such as cavities, channels, or interstices) with the proper size that are interconnected with each other to allow the sound wave to propagate inside the material. Furthermore, water has a great effect on thermo-physical properties, the amount of adsorbed water affects the deterioration process of the material and diminishes its superior insulating effectiveness. In light of the foregoing, it is clear that porous materials are used in a variety of industries, but their morphology has a considerable impact on their performance. Thus pore size and connectivity tailoring are of great importance for different applications.

Among various methods, the application of chemical foaming agents is widely utilized, however, controlling the pore morphology is critical when employing a chemical foaming method. As the previous research indicates, when utilizing foaming agents such as Al, Si, or H_2O_2, pore controlling and tailoring is difficult, both in terms of size and pore cavities formation [1,4,5]. It has been observed that adding surfactants can positively influence the performance of the created foam. Several types of surfactants have been applied in geopolymers, such as Tween 80 [1], Sika Lightcrete 02 [4], Sodium Dodecyl Sulfate (SDS) [6], Triton

---

X-100 [7], Sodium Lauryl Sulfate (SLS) [8] or proteins [9,10]. It is proven that by adding foaming agents and stabilizing agents to the geopolymer slurry, the porosity in the hardened geopolymer can be increased [11–13]. Further, it is revealed that by varying the surfactant and foaming agent concentration, the pore size and size distribution can be adjusted [1]. The samples foamed with hydrogen peroxide and surfactant showed more uniformity in the pore size distribution compared to the samples foamed by sole H_2O_2. An additional benefit is the optimized control of porosity when combining H_2O_2 and surfactant [4].

In terms of density reduction, SLS foam has been considered more cost-effective than protein-based foams [8]. Two non-ionic surfactants that are widely applied in geopolymers are Triton X-100 and Tween 80. Strozi Cilla et al. [7] discovered that an increase in the amount of surfactant (from 2 wt% to 4 wt%) to a metakaolin-based geopolymer leads to an increase in open porosity for both Tween 80 and Triton X-100. Tween 80 forms smaller pores in the geopolymer than Triton X-100, thus contributing to a higher compressive strength of the material. Bai et al. [1] researched the effect of H_2O_2 and Tween 80 on the porosity and compressive strength of geopolymer foam. The positive interaction between H_2O_2 and Tween 80 was observed, which led to highly interconnected pores, good mechanical properties, low density and low thermal conductivity [1]. However, contradicting observations were noted by Petlitckaia and Poulesquen [14], who reported that both Triton X-100 and Tween 80 create heterogeneously distributed pores in the structure with low strength.

Noteworthy, non-ionic surfactant, such as Triton X-100 in combination with ionic surfactants shows better foamability [15]. Despite its remarkable foam-forming characteristics, the system based solely on the non-ionic Triton X-100 has issues regarding foam durability [16]. A similar problem with foam stability has been observed with the use of ionic surfactant, an anionic Sodium Dodecyl Sulfate (SDS), which is a well-known surfactant applied in geopolymers. SDS can be used both as a stabilizing agent and foaming agent [17,18]. However, using solely SDS as a foaming agent results in an unstable foam, despite its strong foaming ability [17,18]. Nevertheless, the use of cationic surfactants, such as Cetyltrimethylammonium Bromide (CTAB), in foams is known to generate low foamability but long-term stability [17,18] even more than non-ionic surfactants [14]. Thus, utilization of surfactants is potentially a promising technique employed in the manufacture of foamed geopolymers. Nevertheless, one problem is its insufficient foam formation efficiency or foam instability. Furthermore, another disadvantage is that a relatively large amount of the surfactant has to be added to obtain highly porous material without providing good pore connectivity.

Considering the fact that the mixed surfactant system displays lower surface and interfacial tension on the same medium than individual surfactants, it is assumed that the combination of two different types of surfactant exhibits synergism [19] or cooperative activity and can also tailor microstructures [15]. Sidim and Arda [20] emphasized the solution's unique features based on the blend of non-ionic and ionic surfactants. Different foamability, foam stability, surface tension, surface viscosity, contact angle, bubble size, and microemulsion stability may be observed when compared to the solution based on individual surfactant. Noteworthy, it is possible to combine surfactants to either obtain a set of desired features or reduce the amount of stabilizing substances used which would reduce the cost and environmental impact of the produced composite.

The above-mentioned properties of mixed surfactants have already been applied in a number of areas, such as Enhanced Oil Recovery (EOR) [21]. However, the beneficial effects of mixed surfactant systems on pore formation in geopolymers have not yet been investigated. Based on the evidence that mixing is beneficial in other fields and the use of single surfactant system is utilized in foamed composites, it is hypothesized that mixing ionic with non-ionic surfactant can improve its performance both at room and high temperature, with the focus on total pore volume, pore size distribution and pore connectivity. Furthermore, the

hygrothermal and mechanical performance are elaborated in order to provide a recommendation towards surfactant mix determining pore structure and its potential application.

This research focuses on designing a biocoal fly ash-based geopolymer for room and high-temperature application, with H_2O_2 as a foaming agent and different surfactant combinations as a stabilizing agent. Moreover, this study specifically aims to investigate the effect of binary surfactant systems on porosity and pore connectivity. Two commonly used nonionic surfactants Triton X-100 and Tween 60, as well as ionic SDS and CTAB, are studied in this research, with the focus on pore morphology determined by microcomputed tomography, mercury intrusion porosimetry and gas permeability, as well as the mechanical, thermal and hygrothermal performance at a humidity-controlled environment coupled with the theoretical calculation of time-dependent heat and moisture transport.

2. Materials and methods

2.1. Fly ash

The raw material used in this research was biocoal fly ash, a byproduct of power generation using coal and biomass as fuel. Biocoal fly ash has a similar chemical composition as Class F fly ash, nevertheless with a higher silica content and relatively lower aluminium content [22], moreover this material contains a higher amount of calcium (Table 1). A laser particle size analyzer (Mastersizer 2000, Malvern Instruments, UK) was used to determine the particle size distribution of the biocoal fly ash, which is depicted in Fig. 1. The three-point specifications of particle size distribution is as follow: $d_{10} = 2.89$ μm, $d_{50} = 19.68$ μm and d_{90} 91.41 μm.

2.2. Alkali activator, foaming agent and surfactants

In this study, an alkaline solution was prepared to achieve a silica modulus of SiO_2/K_2O 1.4 and 5.5% of K_2O by combining potassium hydroxide pellets (VWR Life Science, reagent grade) and potassium silicate solution (WHC, K_2O 8%, SiO_2 20.8%, 72.8% H_2O by mass). Before being used for geopolymer synthesis, the solution obtained was kept unaffected for 24 h to reach equilibrium.

As a foaming agent, hydrogen peroxide (30% Sigma-Aldrich, Germany) was used (see Table 4). Furthermore, four various types of surfactants were used to study their foamability and foam stability in geopolymeric slurries, including anionic, cationic, and nonionic surfactants. Two nonionic surfactants, Tween 60 and Triton X-100 were purchased from VWR Chemicals. Sodium Dodecyl Sulfate (98% purity, Sigma-Aldrich, Germany) was selected as an anionic surfactant, while CTAB (98% Sigma-Aldrich, Germany) is a cationic surfactant. The properties of the used surfactants are presented in Table 2.

2.3. Foamability and foam stability

A fundamental test method was used to evaluate the effect of the mixed surfactant system on foamability and stability, with the details referred to Huang et al. [23] and Pedersen et al. [24]. Deionized water was combined with the surfactant at a mass ratio of 1:5 and was shaken for 1 min. The same weight ratios of nonionic to ionic surfactant were utilized to investigate surfactant interactions in both the aqueous solution and the paste, and they are presented in Table 5. The height of the formed foam was determined after 10 s and 15 min. The above test was conducted twice for each mixture and the results are shown in Table 3. The results indicate that the mixed surfactant systems generate more foam with improved stability, which can be observed explicitly after 15 min. However, it should be emphasized that this test only provides an insight into the synergy between two surfactants in an aqueous solution. When mixed with both Triton X-100 and Tween 60, the SDS system has the highest value of foam height among the analysed systems, both after

Table 1

Oxide composition of fly ash obtained via XRF measurement (in %).

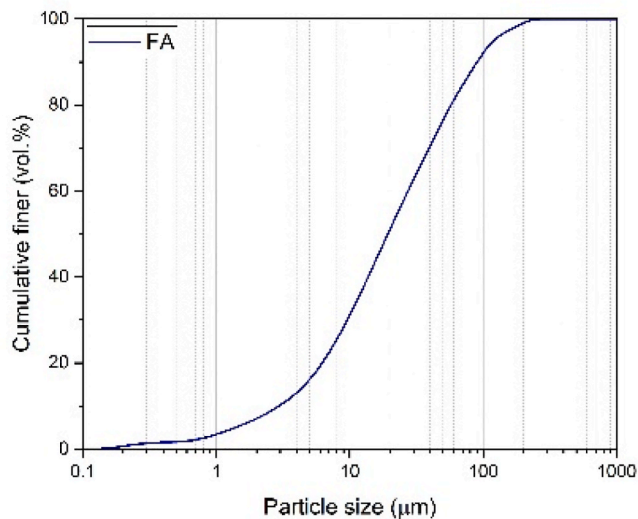| SiO$_2$	Al$_2$O$_3$	CaO	Fe$_2$O$_3$	MgO	K$_2$O	SO$_3$	TiO$_2$	P$_2$O$_5$	MnO	Other	LOI
51.66	18.50	9.62	8.72	2.27	3.68	1.09	1.01	0.82	0.24	0.38	2.01

Fig. 1. Particle size distribution of the biocoal fly ash.

10 s (22 cm and 23 cm) and after 15 min (14 cm and 15 cm). The interaction of these surfactants with one another affects foam formation and stability, either positively or negatively when interactions are synergistic or antagonistic, respectively. The synergism can be attributed to nonideal mixing effects in the aggregates, resulting in Critical Micelle Concentrations (CMC) and interfacial tensions that are significantly lower than theoretical values based on the characteristics of the unmixed surfactants alone. Parra et al. [25] ascribed this to the nonionic agent in those mixed surfactants monolayers that improved the flexibility of the liquid film, which prevented the fracture of the foams.

Noteworthy, the CMC of nonionic surfactants is usually two orders of magnitude lower (Table 2) than that of the corresponding anionic surfactant of the same alkyl chain length and the presence of nonionic surfactants in mixed monolayers enhances the stability of the foam film with certain synergism. The corresponding surfactant combinations in the mixtures and their interactions have been extensively studied

[20,26,27]. El-Aila [28] showed that mixed systems with Triton X-100 both with SDS and CTAB show synergism in surface tension reduction efficiency and mixed micelle formation. Furthermore, Saiad et al. [29] showed that a low CTAB concentration with the dominance of TX100 shows better foaming ability. Based on these findings, it can be assumed that the molecules of both surfactants in the mixture attract each other to produce mixed micelles with different characteristics than the micelle of a single surfactant. In addition, admixing an ionic surfactant with a non-ionic type results in a lower minimum concentration of ionic surfactants. In broader terms, this indicates that less material is required to trigger micelle creation. Referring to the results in Table 3, the blends can be ranked according to their highest foaming and stabilizing abilities in the following order: T60SDS > T100SDS > T100CTAB > T60CTAB. It is worth noting that the cosurfactant system considerably improves the foam's long-term stability, as shown after 15 min (Table 3). However, micelles behaviour in an aqueous solution may differ from geopolymer slurry. A geopolymer paste is considered as a mix of different ions, salts, solid particles which additionally influence those surfactants interactions. For instance, salts tend to screen electrostatic repulsion between the hydrophilic group which makes the surfactant more hydrophobic that leads to aggregation of monomers at lower concentrations, thus lowering the CMC of the system [30].

2.4. Mix proportion and sample preparation

Table 4 shows the mix composition of four geopolymers investigated in the current work. The amount of raw material, activator solution, and foaming agent were kept constant. The geopolymer pastes were prepared by mixing fly ash with the activator solution in a Hobart 5-L mixer. The produced paste was then mixed with the foaming agent, and the resulting mixture was stirred at 150 rpm for 6 min, before casting into the moulds 40 × 40 × 160 mm^3, and 100 × 100 × 100 mm^3. After 24 h, the samples were demolded, wrapped in plastic foil and heated at 65 °C for 4 h before further curing at room temperature.

2.5. Test methods

2.5.1. Calorimetry

The isothermal calorimetry analysis was carried out using an

Table 2

Characteristics of the surfactants applied in this study (data taken from provider).

Name used	Chemical names and category	Linear formula and molecular weight	Trade name	HLB value	CMC (mmol/L^{-1})
SDS	Sodium Dodecyl Sulfate (anionic)	CH$_3$(CH$_2$)$_{11}$OSO$_3$Na M.W. = 288.38	SDS	40.0	8.2
CTAB	Cetyltrimethylammonium Bromide (cationic)	CH$_3$(CH$_2$)$_{15}$N(Br)(CH$_3$)$_3$ M.W. = 364.48	CTAB	21.4	0.96
T60	Polyethylene Glycol Sorbitan Monostearate (non-ionic)	C$_{32}$H$_{62}$O$_{10}$ M.W. 606.8	Tween 60	14.9	0.0167
T100	Octylphenol Ethylene Oxide Condensate (non-ionic)	C$_{14}$H$_{22}$O(C$_2$M$_2$H$_4$O)$_n$ M.W. = 625	Triton X-100	13.5	0.24

Table 3

Mass fraction of nonionic surfactant in total surfactant mix combined with the foam height of single surfactants and cosurfactant mixes measured after 10 s and 15 min.

	Triton X-100	Tween 60	SDS	CTAB	T100 +SDS	T100 +CTAB	T60 +SDS	T60 +CTAB
m$_{nonionic}$/m$_{mix-surf}$	**1.00**	**1.00**	**1.00**	**1.00**	**0.51**	**0.61**	**0.45**	**0.43**
10s (cm)	20	16	21	10.1	22	17	23	12
15min (cm)	5	6	10	6.5	14	13.5	15	9.5

Table 4
Mix proportion of geopolymers (normalized to 100 wt%).

	FA	K₂SiO₃	KOH	H₂O	H₂O₂	Triton X-100	Tween 60	CTAB	SDS	SiO₂/Al₂O₃ (mol/mol)	H₂O/FA (wt./wt.)
T100SDS	72.3	17.1	3.1	6.6	0.5	0.2	–	–	0.2	5.1	0.27
T100CTAB	72.9	17.2	3.1	6.0	0.5	0.2	–	0.005	–	5.1	0.26
T60SDS	72.4	17.1	3.1	6.6	0.5	–	0.1	–	0.2	5.1	0.27
T60CTAB	73.0	17.2	3.1	6.0	0.5	–	0.1	0.005	–	5.1	0.26

isothermal calorimeter (TAM Air, Thermometric), and the heat release during the first 7 days of hydration was monitored at a constant temperature of 20 °C. A certain amount of solid ingredients was first mixed with the alkali activator in the ampoule for 1 min to create a homogeneous paste, which was then immediately loaded into the calorimeter.

2.5.2. Setting time

The setting time was measured with a Vicat Needle apparatus according to European Standard NEN-EN 196-3 [31]. The test procedure considers periodically inserting a standard needle into a cementitious material and analysing its particular resistance to penetration to establish the initial and final setting time.

2.5.3. Mercury intrusion porosimetry

After 28 days of curing, the mercury intrusion porosimetry (MIP) test was carried out on the porous geopolymer. Specimens in size of 3 mm were extracted from the inner part of the specimen, immersed in isopropanol and subsequently dried in a desiccator. The measurements were conducted using an AutoPore IV Series Porosimeter. The applied contact angle of mercury was 130° and the surface tension was 485 dyn/cm. This measurement was conducted to evaluate pores below 5 μm, which is considered as a detection limit for μCT.

2.5.4. Gas permeability

The gas permeability test was conducted on the samples with the size $30 \times 30 \times 50$ mm³ cut from the core of the specimens. The prism-shaped specimen was secured by employing a rubber gasket and a gasket holder in an inflatable sleeve holder to avoid gas (air) bypass between the sample and gasket. By applying the air pressure on one side of the test specimen and calculating the gas flow rate on the other side, it was possible to determine the permeability of the samples by applying Darcy's law.

$$\Delta P = \frac{\eta \cdot L}{\mu \cdot A} Q \tag{1}$$

Where ΔP is the pressure drop, η is the dynamic viscosity of a fluid (air $1.85 \bullet 10^{-4}$ P at 20 °C), A and L represent the area of cross-section and length of the sample, Q is a flow and μ is measured Darcy's permeability.

2.5.5. Bulk density and total pore volume

The volume of the foamed geopolymer was calculated by dividing the mass of the sample, which was cut into cubes, by the geometric volume measured using an electronic height gauge. For each mix, 6 cubic samples were used. The total pore volume was calculated from

$$V_{total} = 1 - \frac{\rho_{bulk}}{\rho_{porefree}} \tag{2}$$

where $\rho_{porefree}$ is the specific density of compacted geopolymer paste obtained via helium pycnometer Accupyc 1330, Micromeritics, Norcross, GA).

2.5.6. Micro-computed tomography (μCT)

Using X-ray tomography, properties including closed pores, distribution of pore size, and 3D reconstruction were determined. The measurements were performed by a μCT scanner (μCT 100, Scanco Medical, Switzerland). The core part of the two samples per mix in the shape of

prism size $20 \times 20 \times 50$ mm³ were analysed. Each prism was analysed at three different heights to provide representative results. A voltage of 70 kV and a current of 200 mA were used for the structure analysis. An aluminium filter of 0.5 mm was applied, and the 2D projection images were created by combining 705 slices which resulted in a 3.52 mm thickness of the composite. Voxel size was determined as 5 μm and the integration time was 220 ms which led to a high resolution of the reconstructed image matrix (2048 × 2048). Using a distance transformation, the data were gathered in 3D visualization form in a 3D model of the sample [32]. The above-mentioned transformation, which consists of filling the empty spaces of the solid component and separating it from the matrix, was applied after the initial identification and separation of the pores from the denser geopolymer matrix and contrast optimization. As a result, the pores and their volume in the VOI (volume of interest) constrained by the specified contour were determined after the identification of all pores on the surface and inside the prescribed contour [33]. To offer a quantitative examination of pore size distribution, the resulting pore size data were recorded as a histogram in the form of a text file. The open porosity and its visualization were calculated from μCT after the separation of the pores. Identified pores were examined for connection to outer contour and between each pore, as well as their volume. To provide 3D visualization, the disconnected pores were separated from the linked pores and displayed in the matrix contour.

2.5.7. Climate chamber conditioning

The test procedure used followed the guidelines stated in ISO 12571:2013E [34]. The measurement was carried out in a climate chamber with an accuracy temperature of 0.1 °C and accuracy humidity of 0.5%. The samples were dried at 105 °C in a drying oven until a constant mass (mass change <0.1%). The climate chamber's specimens were originally preconditioned at the test range's lowest stated humidity level (25%, 40%, 50%, 65%, 80%) at a constant temperature of 23 °C. The samples were consistently weighed until they were in equilibrium
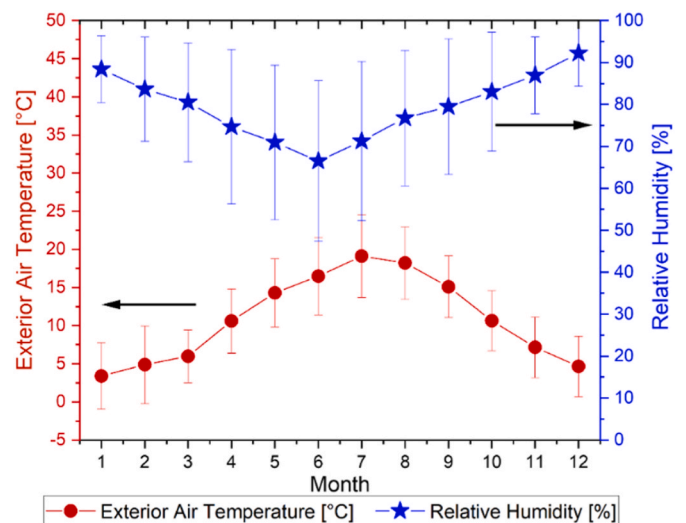
Fig. 2. Temperature and relative humidity profiles for simulated outdoor conditions.

Table 5
Phase quantification via Rietveld refinement of fly ash (error shows in the brackets) (%).

Amorphous	Quartz	Mullite	Hematite	Lime	Potassium carbonate	Magnetite	Periclase	Portlandite	Ammonium sulfate	Calcite	Anatase
ICSD	83849	66451	22505	90486	662	85807	9863	15471	83025	40544	24276
83.9 (0.32)	5.79 (0.09)	3.65 (0.15)	1.95 (0.11)	1.08 (0.05)	1.09 (0.11)	0.70 (0.08)	0.59 (0.08)	0.49 (0.06)	0.28 (0.09)	0.25 (0.06)	0.15 (0.04)

Table 6
Fly ash reactivity based on amorphous Si/Al content.

	Moles of Si per 100 g of FA	Moles of Al per 100g of FA	Si/Al molar ratio
Total content (XRF)	0.8598	0.6857	1.25
Crystalline content (XRD)	0.1133	0.0517	2.19
Amorphous content	0.7465	0.6340	1.18
Extraction	0.4359	0.1497	2.91

with their surroundings (4 weeks). The possible water uptake (η) at different humidity was calculated based on the weight difference between the mass of the sample dried at 105 °C (m_o) and the sample exposed to different humidity at 23 °C (m_1).

$$\eta = \frac{(m_1 - m_0)}{m_0} \times 100\% \tag{3}$$

2.5.8. Thermal conductivity

The thermal conductivity of the samples was measured using an ISOMET 2014 portable heat transfer analyser, which utilizes the ASTM D 5930 Standard Test Method for Thermal Conductivity of Plastics employing a Transient Line-Source Technique. The experiments were run three times on cubic specimens of $100 \times 100 \times 100$ mm^3 at room temperature and two specimens per mix were tested.

2.5.9. Time-dependent heat and moisture content

Hygrothermal performance of each geopolymer composite was further investigated using validated software (WUFI® (Heat and Humidity transient)). The composite was modelled as a single layer wall with a thickness of 4 cm, and their material properties were extracted from the experimental data discussed in previous sections. Transient boundary conditions were imposed on the model; the exterior climate was set based on climatic profile of Eindhoven (Fig. 2), and the interior climate was set as per EN 13788 with humidity class 3. The model was then simulated for a duration of five years.

The transient heat and moisture transport processes are solved by coupled heat transport and moisture transport differential equations

$$\frac{\partial H}{\partial T} \frac{\partial T}{\partial t} = \frac{\partial}{\partial x}\left[\lambda \frac{\partial T}{\partial x}\right] + h_v \frac{\partial}{\partial x}\left[\frac{\delta}{\mu} \frac{\partial p}{\partial x}\right] \tag{4}$$

and

$$\rho_w \frac{\partial w}{\partial \varphi} \cdot \frac{\partial \varphi}{\partial t} = \frac{\partial}{\partial x}\left[\rho_w D_w \frac{\partial w}{\partial \varphi} \frac{\partial \varphi}{\partial x}\right] + \frac{\partial}{\partial x}\left[\frac{\delta}{\mu} \frac{\partial p}{\partial x}\right] \tag{5}$$

respectively, where D_w is the liquid transport coefficient, H the enthalpy, h_v the evaporation enthalpy of water, p the water vapour partial pressure, w the water content, δ the water vapour diffusion coefficient in air, T the temperature, λ the thermal conductivity, μ the vapour diffusion resistance factor, ρ_w the density of water and φ the relative humidity RH.

In the moisture transport model (Eq. (5)), the moisture storage (left-hand term) is directly linked to the water vapour adsorption capabilities, and the moisture transport (right-hand term) contains both the liquid transport and vapour diffusion terms. The pore size and pore structure influence the moisture transport property of a porous material, which can be represented by its hygric properties, i.e. porosity and water vapour diffusion resistance factor. In addition, the variation of climate conditions, particularly exterior climate strongly affects its hygrothermal performance. By including a transient boundary condition, a more realistic simulation of the hygric processes of the geopolymer composites can be assessed, and the simulation results (transient moisture content and U-value) can be further evaluated against the pore structure.

2.5.10. Compressive strength

The compressive strength was evaluated according to EN 196-1 [35]. At the ages of 7 and 28 days, cubic samples ($40 \times 40 \times 40$ mm^3) were tested. The loading rate is 1000 N/s, and the compressive strength is calculated as the average of six test results.

3. Results

3.1. Raw material characterization and activation

The XRD analysis (Table 5) reveals that the biocoal fly ash is highly amorphous (85%). Thus, the approach suggested by Sanalkumar et al. [36] was used to assess the reactive molar Si/Al ratio of the raw material. 200 ml of NaOH (10 M) and 7.5g of biocoal fly ash were mixed and stirred at 80 °C for 2 h. Subsequently, the inductively coupled plasma atomic emission spectroscopy (ICP-OES) analysis of the filtrate was performed. Additionally, the liquid filtrate was also examined by
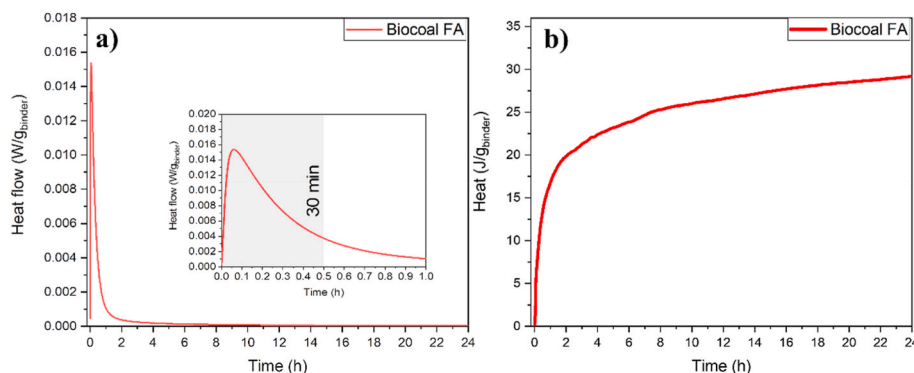
Fig. 3. Isothermal calorimetric response of biocoal fly ash geopolymer pastes at 20 °C a) normalized heat flow, and b) normalized cumulative heat.

ICP-OES after the solid residue from NaOH treatment (2g) had been mixed with 500 ml of hydrochloric acid (32%) for 3 h. The sum of the eluted silicone and aluminium obtained via ICP-OES was applied to determine the reactive Si/Al ratio. In Table 6, the comparison of the Si/Al ratio obtained by the various method applied in this study is presented. Based on the obtained results, the reactive Si/Al ratio is 2.91.

The setting time of alkali-activated material is highly related to the reaction temperature, a small increase of the temperature shortens the time significantly. The initial and final setting time measured for alkali-activated biocoal fly ash were 16 min and 48 min, respectively. During the hydration reaction, the BCFA possesses a relatively high heat release, which indicates a strong exothermic reaction (Fig. 3a), which in consequence reduces the setting time. The observed exothermic peak corresponds to the wetting, dissolution-precipitation, which appeared within the first hour and was common in both samples regardless of raw material source. Due to the relatively low reactivity of the ash sample at ambient temperature, after dissolution peak, the line tends to follow straightly horizontally. Observed phenomenon might be owing to the slow rate of reaction. As found by Nath et al. [37], fly ash geopolymerization is a process in which the reaction proceeds for a longer duration with low heat evolution after precipitation (Fig. 3b).

Noteworthy, the evolution of a minor amount of $NH_{3(g)}$ has been observed through the ion chromatography analysis. The gas released within the first 10 min was captured in an aqueous solution which was then analysed for NH_4^+ ions. NH_3 can be found as molecules adsorbed on the surface of ash particles, forming chemical bonds at active sites, and also as an ammonium salt (mostly sulphates and bisulphates) that adheres to grain ash [38]. Moreover, the presence of free lime (Table 5) and the addition of alkali accelerates the NH_3 release. Furthermore, the production of K_2SO_4 is confirmed by XRD. Fig. 4 presents the XRD results of raw material and reaction products after 30 min of activation (Fig. 3a). The primary finding is the consumption of calcium oxide and ammonium sulfate (shown by the arrows in Fig. 4) and the appearance of a new potassium sulfate phase, as a result of a highly alkaline activator solution that contains KOH. The above XRD analysis of geopolymer reaction products supports the findings of calorimetry and a potential explanation of factor inducing quick flash setting of the matrix.

Nevertheless, it should be highlighted that for the analysed porous matrix it is beneficial to have a short setting time, which provides less time for the bubble collapse to occur and the influence of the setting time on the Ostwald ripening and pore collapse can be minimized. In many studies, the use of nucleating agents that accelerate the setting and
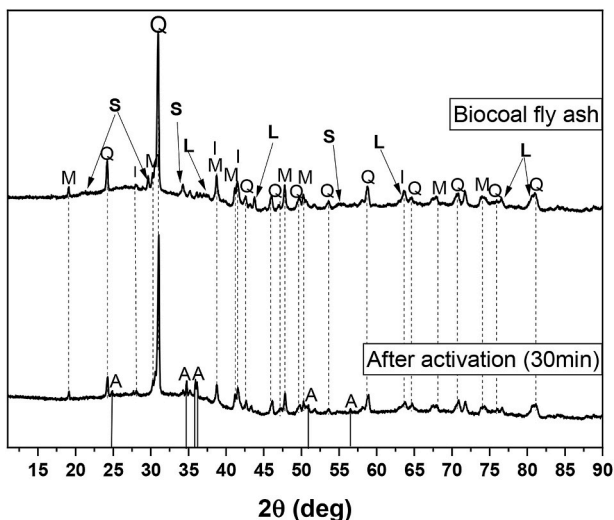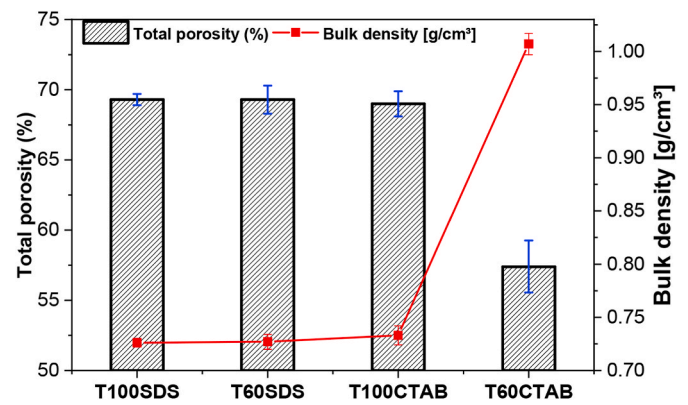
Fig. 5. Total porosity and bulk density of porous geopolymer pastes.

reduce the extent of air bubble collapse are recommended [4].

3.2. Density and total porosity

The composites produced with a reduced quantity of a foaming and stabilizing agent (Table 4) by the aeration process were characterised in terms of aeration efficiency. Thus, the overall porosity and bulk density of the collected porous geopolymers are depicted in Fig. 5. These values show that the three chosen blends have a comparable porosity. T60CTAB, on the other hand, has a significantly lower porosity (e.g. 11.9% less than T100SDS). Comparing the foaming information in Table 3 with the obtained porosity, it can be seen that the observed heights after 15 min, and more precisely the approximate values of the foam heights between T100SDS, T100CTAB, and T60SDS, as well as the significantly lower value for T60CTAB, are in agreement. One probable explanation for T60CTAB is that, due to the relatively high surface tensions of the cosurfactant, it is not feasible to increase the surface area to facilitate foam production, resulting in poor foamability [20,27,39, 40].

It can be observed that both non-ionic surfactants (TX-100 and Tween 60) combined with anionic surfactant SDS produce a more porous structure characterized by a low bulk density ~ 0.7 g/cm³, thus SDS shows good foamability properties. Korat et al. [41] investigated fly ash-based geopolymer in which one type had similar content of hydrogen peroxide (0.5%) and SDS 1%. The obtained density and porosity were 1.08 g/cm³ and 24.2%, respectively. In our case, the addition of 0.1% of Tween 60 or 0.2% of Triton X-100 together with SDS (0.2%) results in a material with obviously lower density (0.7 g/cm³) and higher porosity (~69%). Another research [14] utilizing the same foaming agent (H_2O_2) and surfactant (CTAB) achieved a similar density of 0.6 g/cm³, which, however, applied a much higher concentration of CTAB (0.05% vs. 0.005%) than in this study. Furthermore, Xu et al. [42] produced a comparable composite density using 2.5% H_2O_2, but the pore structure was optimized using 3.5% H_2O_2 and 2.85% SDS. Increasing the amount of foaming agent to 1% and using 3% SDS resulted in a similar density of 0.63 g/cm³ [43], indicating that the mixed system contributes to reducing the amount of foaming agent and surfactant used while achieving similar values of density and volume of pores.

3.3. Open porosity

The influence of the co-surfactant mix on the formation of pore cavities is analysed in the following section based on the above-discussed total porosity value. The evaluation is carried out based on the μCT analysis. Firstly, the image processing is performed by using an IPLFE v1.16 (Scanco Medical AG, Switzerland) to determine the open pores. The procedure is described in-depth in the methodology section. The potential for fluid (e.g. water vapour) movement through the

Fig. 4. XRD diffractograms of raw material and reaction product with marked only the most significant phases. Legend: **Q** Quartz; **M** Mullite; **I** Iron oxide; **L** Lime; **S** ammonium sulfate; **A** Arcanite.

structure is evaluated to examine principally porosity using a computer microtomography and utilizing the gas permeability technique and mercury intrusion porosimetry for the volume of open pores and distribution of pore size respectively.

The pore separation demonstrates (Fig. 6) that in all of the pastes based on nonionic surfactant and cationic CTAB, the closed pores are more prominent, which is more prominent in T60CTAB, where the open pores account for 32.4 vol %. It is evident that the samples with similar total porosity, namely T100CTAB, T100SDS, and T60SDS (Fig. 5), are distinguished by a different value of open porosity, which is driven by the used surfactant.

Alteration is noted in the overall volume of the pores, their size, and distribution in the structure, i.e. the distances between the pores, depending on the mix of surfactants utilized. With a high porosity, a wide range of pore diameters, and dense packing of the bubbles, cavities between the pores might develop, defining the open porosity. Section 4.1 is devoted to revealing the mechanism that promotes the development of two different types of pore structures under the premise that morphology is mostly driven by the type of used ionic surfactant in the mix. It is presumed that CTAB-containing mixtures have a higher paste viscosity [14,44], which is due to substantial CTAB adsorption on fly ash particles. This strong interaction influences the gas-liquid interface, providing a rigid film that hinders the passage of gas between bubbles, resulting in an observable thicker distance between wall pores, and reducing the chances of the pores coming close enough to be able to create an opening in their wall and build a connection [14].

Lu and Qin [45] evaluated the porosity development of a fly ash-cement mix and discovered that, despite getting a similar value of total porosity (~70%), the volume of open pores was substantially lower (37%) than those in our study (48% for T60SDS and 53% T100SDS). Furthermore, Strozi Cilla et al. [7] reported similar open porosity, but with a greater quantity of single-surfactant added to the geopolymer slurry: with 2 wt% of Triton X-100 or Tween 80 added, they discovered open porosities of 50% and 54%, respectively.

The findings of the µCT evaluation are supported by the gas permeability coefficient. The high material permeability implies good fluid movement through the pores. For high temperatures applications, as described above, it is desired to minimize the damage by cracking and spalling caused by the transport of water vapour through the structure. The highest value (8.1×10^{-13} m^2 = 0.83 D) was obtained for T100SDS, which has the greatest value of open pore volume. T100CTAB and T60SDS were distinguished by relatively lower permeability coefficient values (3.7×10^{-13} m^2 (0.38 D) and 4.1×10^{-13} m^2 (0.42 D), respectively). The results are in agreement with open porosity results, also for the mix based on T60CTAB the permeability was established as 2.8×10^{-13} m^2 (0.29 D). These values fall within the classified gel casting foams' permeability between 10^{-13} and 10^{-9} m^2 [46]. Airflow in porous materials is a volumetric phenomenon that is largely dependent on pore size, thus with decreasing solid volume fraction, as well as increasing in pore size, Darcian permeability increases. The pore size distribution of T100SDS and T60SDS is shifted towards a bigger size than T100CTAB,

thus causing a higher air permeability. Therefore, it is concluded that an improved permeability of the composite is resulted by applying non-ionic surfactants, both Triton X-100 or Tween 60, together in combination with SDS.

In order to assess the efficiency of the proposed method, the obtained results were then compared with the literature, which also present the method of obtaining foamed geopolymers with the use of surfactants such as SDS, oil, or proteins. Fig. 7 depicts the relationship between the total and open porosity. Bai et al. [47] presented intriguing results in which the volume of open pores to total porosity ratio is close to 1: 1 as foaming agents, H$_2$O$_2$ (3%) and olive oil were used. Yan et al. [43] observed a high ratio of open porosity to total porosity (86.9 vol%) using SDS (3%) and H$_2$O$_2$ (3%) that can be compared to the present T100SDS result, which has a much lower fraction of foaming agent (0.5%), as well as total surfactant content. As can be seen in Fig. 7a, as porosity increases, the air bubbles are packed more closely together, thus increasing the probability of open cavities formation. For the total porosity range close to the composites T100SDS, T100CTAB, and T60SDS (see Fig. 7b), it can be seen that the obtained results are promising in terms of the content of open porosity in total porosity as well as the amount of utilized surfactant. Noteworthy, the total porosity and open cavities of the material should be chosen based on its intended application. Further, it should be taken into account that as porosity increases, the mechanical resistance of the material decreases [51].

3.4. Pore size distribution

Aside from total and open porosity, the distribution of pore size in the structures determines the strength or hydrothermal properties of the composites, as well as the ability to generate pore cavities due to their way of packing in the matrix. Attention should be paid to air voids, macropores, and mesopores in order to track variations in the pore structure of the resulting composites. The µCT measurement covers the macropores, which are the main product of the chemical aeration of the structure, while the MIP was used to examine the pore nature between 5 nm and 5 µm.

3.4.1. µCT

The pore characteristics are determined by using µCT on the samples (size $20 \times 20 \times 50$ mm^3). This analysis helps to understand the composite microstructure, the pore size and their distribution in 3D. To focus on the details of the pores of geopolymers created as a result of the proposed chemical aeration, the observed values are presented in Fig. 8. The pore distribution is generated by combining total pores and pores determined by µCT, with a detection limit of 5 µm. Based on these graphs, it is clear that CTAB-based systems favour low-sized pores, whereas SDS provides the majority of pores above 200 µm. The pores above 200 µm overall for T100SDS and T60SDS comprises accordingly 56.1% and 50.6% in the normalized total porosity, while for T100CTAB and T60CTAB 23.2% and 14.3% respectively. In both CTAB-based systems, regardless of the type of nonionic surfactant, a majority of pores
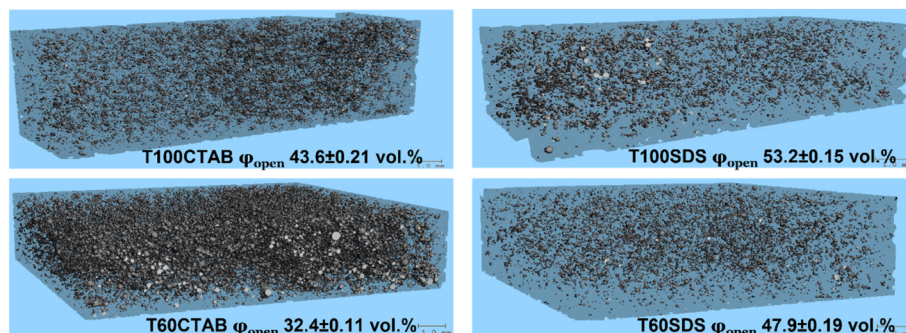

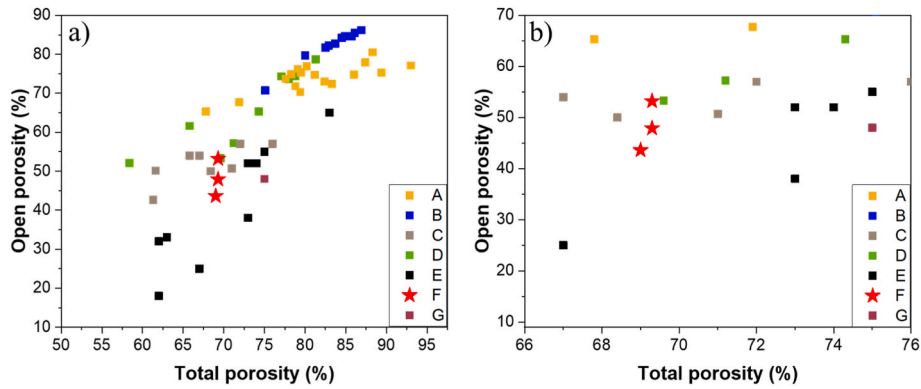**Fig. 6.** Visualization of the specimens with marked closed pores.

Fig. 7. Open porosity vs total porosity of designed composites and other foamed geopolymers. A [43]; B [47]; C [48]; D [9]; E [49]; F:this study; G [50].

between 50 and 200 μm, as well as the higher contribution of pores between 5 and 50 μm is observed.

It can be observed that Tween 60 directs the formation of small size pores (<5 μm) more effectively than Triton X-100 (23–25% in total pore range). Moreover, when T60CTAB and T60SDS are compared, it is clear that Tween 60 creates small pore sizes, which is comparable to the effect derived by pure CTAB. Both Tween 60 and CTAB surfactants boost the formation of small pores, reducing the possibility of Ostwald ripening and merging air bubbles.

The existence of pores in specific ranges has different impacts on performance such as heat conductivity and water suction. Small-diameter closed pores contribute to smaller thermal conductivity, simultaneously partially open small pores will increase water transport in the material's structure, whereas large pores increase the probability of open porosity and the contribution of pore radiation in the total heat transfer balance should not be omitted [52].

3.4.2. MIP

Further, to analyze the nature of the pores smaller than 5 μm, mercury intrusion porosimetry (MIP) analysis was performed. Despite the different nature of the measurement compared to μCT and the values

obtained by the two methods, the trend among the four specimens is maintained. Fig. 9 also shows the calculated values obtained through the μCT route and the porosity obtained as bulk porosity. In the case of T100SDS and T60SDS, the values are higher than expected, which may be related to the smaller distance between the bubbles, resulting in thin walls of interfaces that could have been damaged during the pressurized mercury intrusion. While in T100CTAB and T60CTAB lower values are noticed, suggesting greater material stability, thicker pore walls and the presence of closed pores unable to be filled with mercury. However, due to the variety of throat size and "ink bottle" effects, MIP measurements may misallocate the pore diameters, assigning them to sizes lower than the real ones [53].

Pores between 0.005 and 1.0 μm present in the geopolymerization product can be classified as gel pores (<0.01 μm) and capillary pores (0.01–1 μm) [54]. The four analysed samples constitute of similar contribution of pores (0.005–1.0 μm) due to the geopolymeric gel structure of the composites. Furthermore, T60CTAB is characterized by a greater content of both 0.005–0.05 and 0.05–1.0 μm pores, which confirms the hypothesis of the formation of pores below 5 μm, determined by the presence of both Tween 60 and CTAB. The influence of CTAB on the formation of smaller size pores can be also observed in
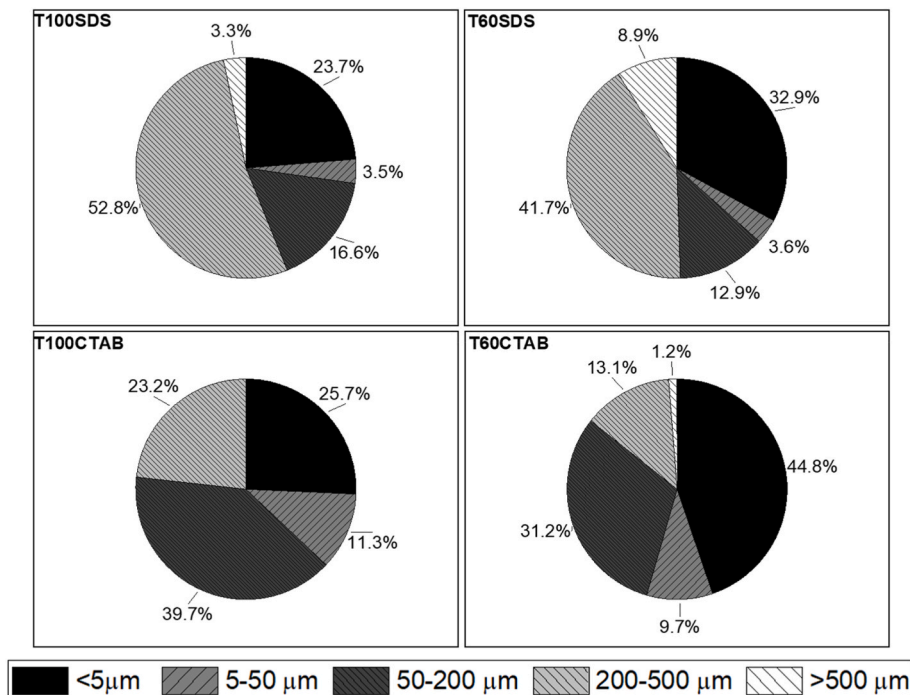

Fig. 8. Pore size distribution of the porous specimens in the range >5.0 μm.
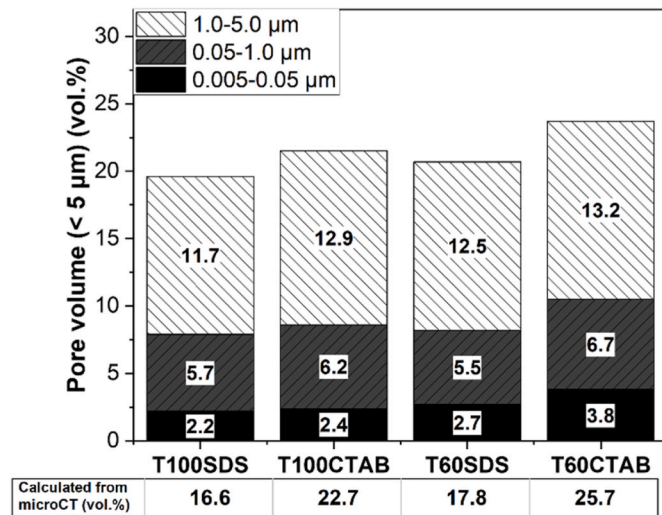
Fig. 9. Pore size distribution within the range 0.005–5 μm obtained via MIP method. Below the graph calculated values of pore volume below 5 μm obtained via combined bulk porosity and μCT method are presented.

T100CTAB.

3.5. Hygrothermal performance

3.5.1. Steady-state state

Several material parameters, such as bulk density, porosity, thermal conductivity, and vapour permeability play a significant role in hygrothermal performance evaluation [55], and the properties of the resulting composites differ from one another (Figs. 5 and 6). As the humidity in the atmosphere rises, materials become partly saturated with water, negatively impacting thermal conductivity [56]. Noteworthy, the size, tortuosity, and type (closed/open) of pores are crucial in water transport through porous structures [57]. The permeability and diffusion coefficients rise as porosity and pore size increase. Therefore, the water vapour adsorption capacity is monitored for three out of four mixes due to their similar total porosity (~69%), providing an insight into the influence of pore size and pore connectivity on the hygrothermal behaviour of foamed geopolymer (Fig. 10). It is well established that with the increased total porosity, the water adsorption increases. The sole transport mechanism at very low RH is vapour transfer. The number of layers of water molecules on the surface grows as air humidity rises and firstly small size pores are filled and then connected bigger pores are occupied with a single layer of H_2O. As demonstrated by Kato et al. [58], with an increase of open porosity water adsorption rise can be expected.

Conducting a thorough analysis of the three established metrics concerning pore size, open porosity, and permeability helps to comprehend the variances caused by the quantity of adsorbed water. It can be stated that among the three samples (T100SDS, T60SDS, and T100CTAB) characterized by a total porosity of ~69 vol%, the T60SDS sample has the highest proportion of small pores below 5 μm (Fig. 8), and up to 10% greater than the T100SDS sample, whose pores are firstly filled with water. When the relative humidity reaches 40%, water may be present in both small (5–50 nm) and big pores (>50 nm) [59], then the key role open porosity plays on permeability can be observed as a significant increase between RH 40% and 50% in T100SDS. It is in agreement with the observed results when combined with the open porosity, which rises in the sequence T100SDS > T60SDS > T100CTAB. T60SDS has the largest degree of water content at RH 40%, while at higher percentages of humidity, a stronger influence of permeability and open porosity on the passage of water vapour into the matrix is observed. This phenomenon can explain the minor difference between T100SDS and T60SDS at higher humidity.
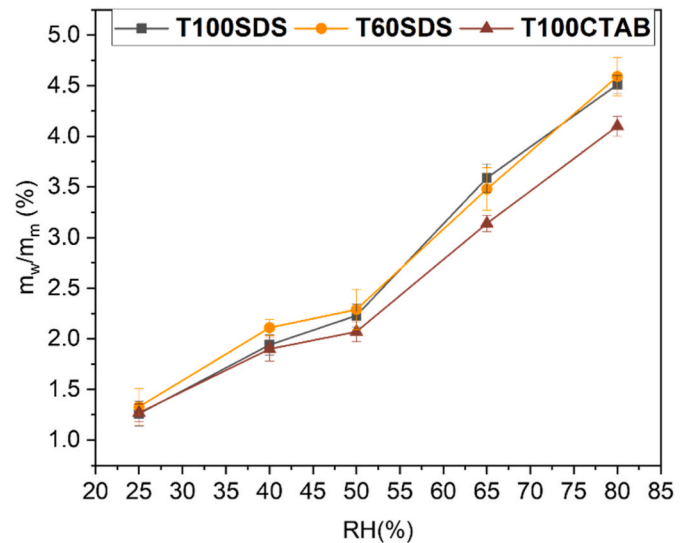

Fig. 10. Water uptake depends on the controlled relative humidity in the climate chamber.

High pore connectivity, and hence high gas permeability, is inversely proportional to tortuosity, which influences the fluid flow rate [60]. As a result, fluid (moisture) flow is more hindered in the sample characterized by low gas permeability, for example, T100CTAB compared to the SDS-based mixes. Additionally, the connection between pores above 5 μm in T100CTAB is limited, as illustrated in Fig. 6, and a considerable number of small size isolated pores densely packed in the structure is observed. Furthermore, more connectivity paths can be created by increasing the size of the pores [61]. When compared to composites with a predominance of small pores, the pore size increases the ability of media to pass more fluid through a porous matrix [62]. The sample T60SDS represents the material with a high proportion of pores smaller than 5 μm (Fig. 8), high pore volume connectivity and permeability, all of which play a crucial role in low humidity environments (RH = 25%) (Fig. 10).

Thermal properties are critical for thermal insulating or fire-resistant materials. It is known that the heat conductivity of porous materials is affected by a variety of factors. In addition to overall pore volume, the pore size distribution, homogeneity, and opening level of pore cells also have an impact [52,63], nevertheless, the thermal conductivity of the solid matrix and total porosity are the two dominant factors [64]. Porous materials with excellent thermal insulation properties are characterized by closed pores, which limit the heat flow of gases, and therefore T100CTAB sample, which, although having a similar total porosity as SDS-based samples (Fig. 5), has a smaller percentage of open porosity (Fig. 6). The lowest amount of overall porosity determines the maximum value of thermal conductivity for T60CTAB.

Total porosity and matrix conductivity show the largest influence on the effective thermal conductivity, which is the reason for the minor change between samples T60SDS > T100SDS > T100CTAB (Δλ: 0.009–0.02 W/mK). However, the densely packed isolated pores above 5 μm define the better performance of T100CTAB than T60SDS. Chen et al. [65] stated that for the same porosity, the smaller the pore size, the greater the number of pores, and the lower the heat transfer efficiency. T60SDS has a larger content of pores above 500 μm (8.9 vol%) than T100SDS (3.3 vol%) and T100CTAB (0 vol%), resulting in improved heat transmission and increased thermal conductivity.

Conditioning composites at varying humidity levels allowed us to assess not only their sorption capacity but also their steady-state thermal conductivity at a particular moisture content. Fig. 11 depicts the obtained experimental values of effective thermal conductivity acquired after exposure to a controlled humidity chamber. Consequently,

materials' ability to adsorb moisture varies, their thermal characteristics in a saturated condition differ significantly (Fig. 11). T60SDS and T100SDS exhibit poorer thermal insulating capabilities (higher lambda) over the whole range of moisture content due to their greater volume of open pores (Fig. 6) and higher initial thermal conductivity value in a dry state (Table 7).

3.5.2. Transient state

The hygrothermal performance of each geopolymer composite was further examined using a WUFI® (Heat and Humidity transient) software. Simulated results under the fifth year were extricated and used as a case study for subsequent discussion here.

Fig. 12 depicts the monthly averaged water content inside the geopolymer composites throughout a simulated year. Lower water content for the T100CTAB composite is observed in the range of 2.7% and 4.8%, in comparison to T60SDS and T100SDS where higher water contents are obtained. These simulated results have verified the proposition from the earlier experimental study, i.e. closed pores in a composite will reduce its water uptake capability, which coincides with T100CTAB that has a lower water content under ambient climatic conditions with its higher closed pores structure. Furthermore, all three developed geopolymers have a consistent course in their water content throughout a year, with only slight fluctuations represented in the form of deviation bars in Fig. 12. These stable trends show these three selected composites are effective in transporting water vapour, which further suggests that they can be potentially used to regulate the surrounding humidity fluctuations when used as wall assembly.

The transient thermal transmittance of the composites during the heating period (October to March) are summarized in Fig. 13. Additionally, the thermal transmittance at 80% relative humidity for each composite are included in the same plot, represented by dash lines for reference purpose. Due to their aforementioned ability to easily absorb and desorb water vapour from the surrounding air, all three geopolymers exhibit good thermal insulation performance and did not surpass their 80% humidity threshold. Their simulated transient thermal transmittance is also in agreement with the assumption derived from the thermal conductivity experimental study, with T100CTAB being the better insulating material, followed by T100SDS and T60SDS.

For comparison purpose, two commonly used commercial building materials are included in the simulation, namely gypsum plaster and cement lime plaster, both have similar applications as the developed geopolymers. A noticeable pattern can be straightaway observed from Fig. 13, where a larger range of thermal transmittance is gained by both
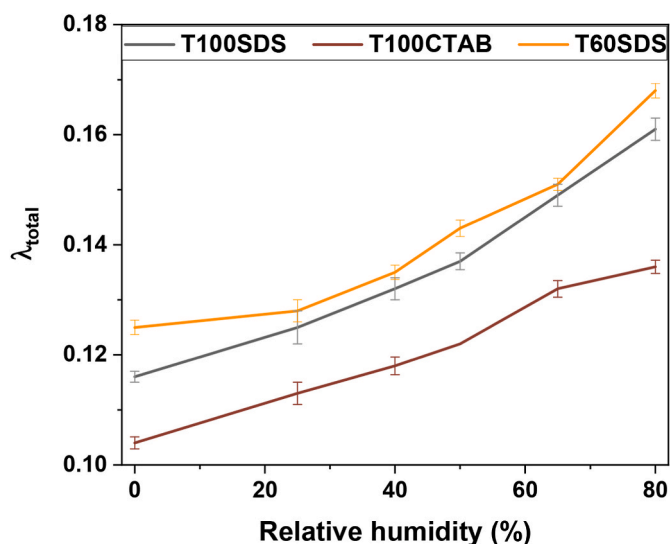
Table 7
Thermal conductivity of the foamed geopolymers.

Groups	T100SDS	T100CTAB	T60SDS	T60CTAB
λ (W/(m·K))	0.116 ±0.002	0.104 ±0.003	0.125 ±0.001	0.146 ±0.001

commercial materials, with a major part of their heating period suffering thermal transmittance worse than their value at 80% humidity threshold. This is differing from the better and steadier thermal performance of the developed geopolymers. The main plausible cause is that the geopolymers have better ability to regulate changes in relative humidity than the plasters (Appendix Figs. C, D). Another lesser element in play may be due to the water vapour diffusion resistance factor (μ) of investigated materials, where the geopolymers have a lower μ value in comparison to gypsum and cement lime plasters, i.e. the lower μ geopolymers have less resistance in preventing moisture transport throughout the material and consequently minimize the risk of accumulating higher water content inside the substrate.

3.6. Compressive strength

In order to preserve their mechanical stability and integrity, alkali-activated foams need sufficient mechanical strength. However, as already noted, a flash setting has been observed in the investigation that has a detrimental impact on material strength growth over time and consequently low strength values are seen for all mixes. Overall, the obtained results suggest that the geopolymer matrix and pore shape determine the mechanical strength and the structural stability of the composites was influenced by pore size, distribution and cell-wall thicknesses.

It should also be noted that an increase in the median pore diameter has a detrimental impact on the composite's strength. The pore distribution plots of T100CTAB and T60CTAB demonstrate a shift towards lower values (<200 μm) than the SDS-based systems, thus a higher fraction of pores with a diameter below 200 μm mitigates the porous structure's negative impact on compressive strength (Table 8). With the same pore volume, the sample with larger pores has lower strength, as observed in the T60SDS and T100SDS (Table 8). Regarding the pore connectivity, as stated by Ji et al. [61], pores smaller than 200 μm have a reduced possibility of collapsing due to their greater distance from one another when distributed in the same volume as pores of larger diameter provide a less fragile matrix backbone, contributing to the increased strength of composites.

Fig. 14 plots the compressive strength versus porosity of foam geopolymers made from various materials [66]. The fitting curve has been developed using the Ryshkevich model [67] based on the findings by Fiset et al. [49]. It demonstrates that the relationship between compressive strength and porosity may be accurately predicted at the porosity above 75 vol% (region II), and large variations are seen in the lower porosity region (55–75 vol%, region I). In region I, pore size distribution is more important than total porosity in the evolution of mechanical resistance. A narrow and small pore size distribution improves the mechanical performance of the composite, as emphasized by Ji et al. [61]. Above this range (region II), the total porosity increases due to the increased volume occupation by air/gas phase, resulting in a decrease in total amount of solid matrix. As a result of the insufficient solid volume fraction, the overall mechanical strength in region II decreases.

According to Zhang and Wang [68], it is better to predict mechanical performance using pore volume above 100 μm rather than total porosity, since there are more substantial variations in mechanical performance. Comparing the obtained results with the literature it can be observed that the material is characterized by relatively low compressive strength, which is mainly due to the low raw material reactivity and high content of large air voids and relatively high open
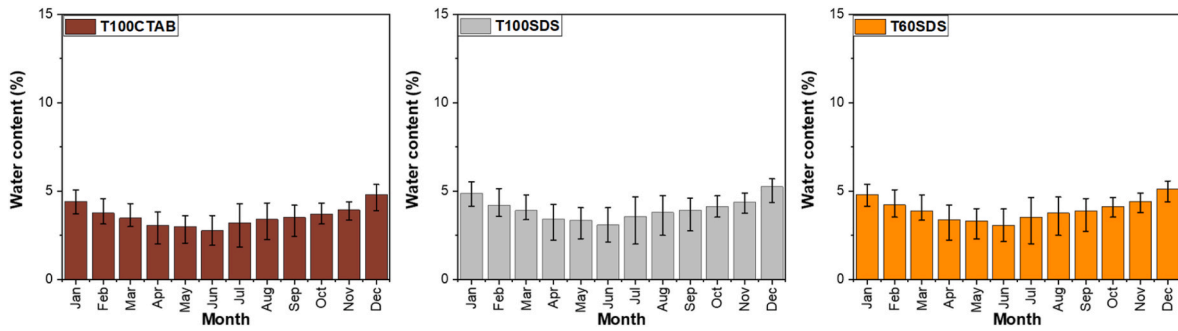

Fig. 11. Effective thermal conductivity as a function of relative humidity.

Fig. 12. The moisture content of geopolymers section in the 5th year under one climate condition. With marked min and max values of water content reported in each month.
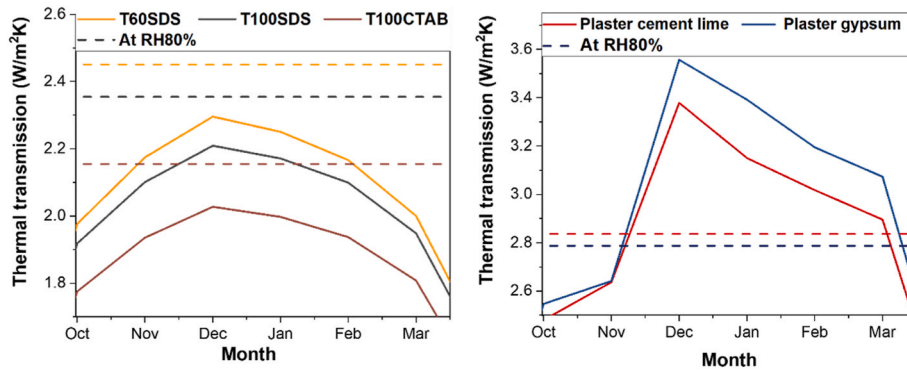

Fig. 13. Transient U-value of the designed porous materials compared to two commercially available products under one selected climate profile.

Table 8
Collect data on porosity, pore size, and compressive strength.

	Pores <200 μm (vol%)	Pores >200 μm (vol%)	Compressive strength (MPa)	Open porosity (vol %)
T60SDS	34.3	35.0	1.38	47.9
T100CTAB	53.0	16.0	2.51	43.6
T100SDS	30.4	38.9	1.16	53.2
T60CTAB	49.2	8.24	3.67	32.4

porosity (Fig. 7). Dhasindrakrishna et al. [69] proposed that curing at higher temperatures may be used to increase the early age strength, and the findings revealed that compressive strength of foamed geopolymer samples after high temperature can reach up to 3.5 times that of the equivalent unexposed geopolymer samples.

4. Discussion

4.1. Mechanism governing pore structure alteration

Surfactant adsorption has been seen not only on the gas-liquid interface but also on the liquid-solid contact. Adsorption on the surface of solid particles happens as a result of electrostatic interaction for ionic surfactants [80] and through hydrogen bonds for non-ionic surfactants. The schematic diagram of the proposed mechanism is presented in Fig. 15. Geopolymer paste can be considered as a matrix loaded with solid particles, polyvalent ions, and negatively charged solid particles as a result of a very alkaline environment. The negatively charged surface of the ash particles absorbs the cationic surfactant at a high pH (CTAB) [81]. The interaction between the surfactant molecule on the surface of the air bubble and the charged particle will result in high bubble surface stability, reducing the possibility of coalescence [82–84]. The scenario is different for anionic surfactants, as SDS is not as
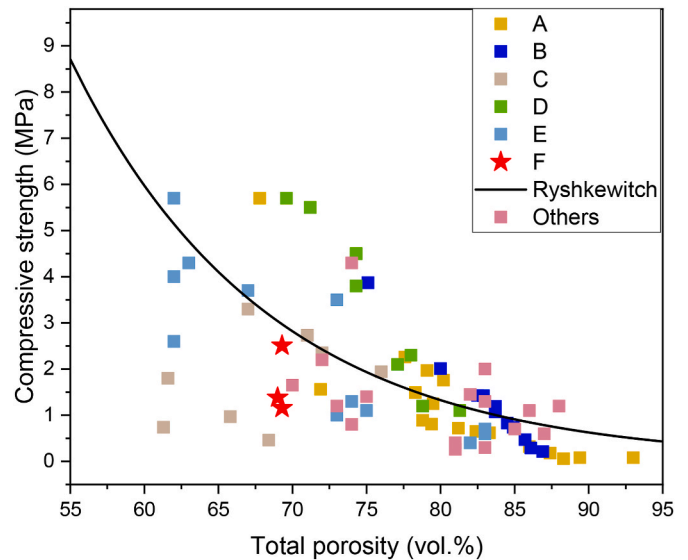

Fig. 14. Compressive strength vs porosity of various geopolymer foams. A [43]; B [47]; C [48]; D [9]; E [49]; F:this study; Others [51,70–79].

strongly attracted to negatively charged particles; nonetheless, the existence of multi-positive ions, such as calcium, can act as a bridge between the negatively charged solid and the surfactant molecule (Fig. 15). To conclude, SDS interactions are substantially weaker than cationic CTAB interactions, which impacts the ability to adhere bubbles or appear in extremely close contact, while maintaining greater stiffness at the liquid-vapour boundary than in non-enriched air bubbles, which promotes the formation of pore cavities.

The non-ionic surfactant is another component of a binary system
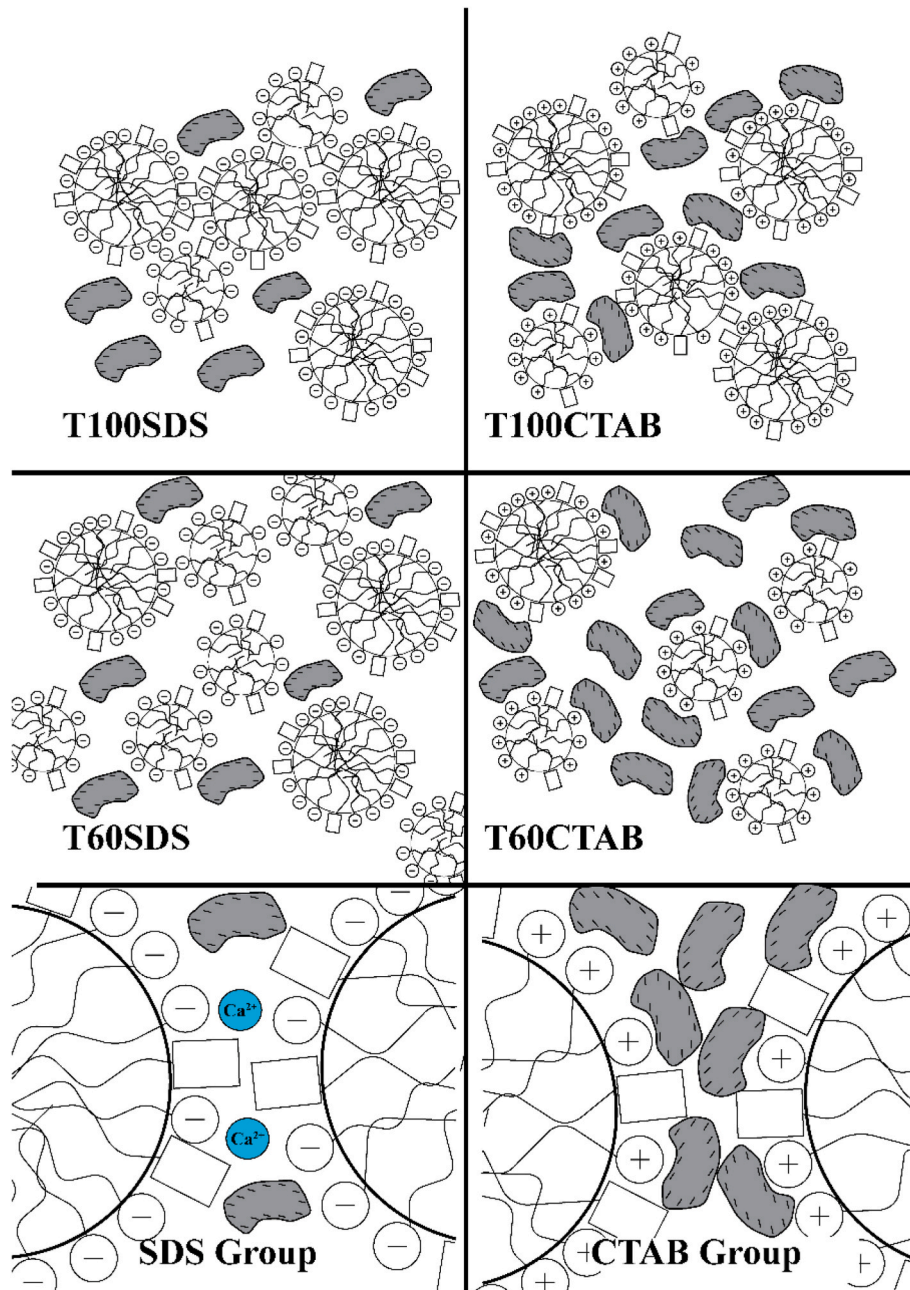
Fig. 15. Interaction mechanism between air bubbles stabilized by different binary surfactants mix and fly ash particles (grey) governing pore connectivity. Note: Ca^{2+} represents various bi- and polyvalent ions in the systems.

(Tween 60 and Triton X-100). Because they are non-ionic, these surfactants do not adsorb strongly on charged surfaces. This reduces the unwanted loss of surfactant access at the solid-liquid interface while increasing surfactant availability at the liquid-vapour interface to saturate that surface [85]. Non-ionic surfactants exhibit the lack of characteristics required for appropriate air bubble stabilization, resulting in coarsening and coalescence. However, in a binary system with ionic surfactants, non-ionic Triton X-100 or Tween 60 can boost the solubility of ionic surfactants in the binary (cosurfactant) system and diminish the ionic surfactant's tendency to adsorb at the interface solid-liquid interface [85]. In the case of SDS-containing systems, a synergistic co-adsorption is proposed, in which a marginal co-adsorption occurs on negatively charged surfaces of mixed micelles even though SDS alone would not adsorb [86]. Moreover, adsorption of anionic SDS on polyvalent cations increases at higher pH, thus a bridging effect between the

negatively charged surface and SDS via cation can be observed (Fig. 15) [87,88]. Although, as explained above for the CTAB scenario, this interaction may contribute to the improved stabilization of air bubbles in anionic-contained mixtures. However, interaction in a mixed system cationic-nonionic entails poorer interactions with negatively charged particles in a solution containing a cationic CTAB, as well as the potential of links between air bubbles close enough to form cavities.

Moreover, because of the synergism between the surfactants used and the lower CMC_{mix} value compared to pure ionic surfactant, the micelles formed in large quantities can be tightly packed in the structure, and the described properties of disjoining pressure prevent excessive aggregation and bubble rupture. When the thin liquid film evaporates, connections between the pores, small cavities in the thin walls separating the bubbles, may form in both systems based on CTAB and SDS. This phenomenon is owing to a decrease in surface tension

caused by more migration of nonionic surfactant to the surface layer and a reduction in electrostatic self-repulsion between head groups in the ionic surfactant (Fig. 15). Additionally, the variation in the pore size can be expected, due to the different hydrophilic group structures [89]. Furthermore, the surfactant, which creates lower surface tension, is responsible for creating finer air bubbles [90]. This explains why Tween 60 results in lower pore sizes (a high fraction of pores less than 5 μm) in both T60CTAB and T60SDS (Fig. 8).

4.2. Potential application areas driven by pore size and connectivity

Based on the present results, it is feasible to construct a list of morphological traits, and more specifically, pro-quality features and potential of various application areas. Table 9 depicts the primary pore morphological traits that suggest the potential for usage in areas such as high temperature, fire protection, thermal and acoustic insulators. Materials with a predominantly closed porosity are better thermal insulators than open structures attributed to the facilitated flow of heat through cavities. Therefore, the T100CTAB with the lowest thermal conductivity coefficient value can be chosen as a thermal insulator.

The composites used in this work are made of a solid aluminosilicate skeleton which provides high-temperature stability [2]. In addition to the beneficial effects of the chemical and mineralogical composition, the role of open-pore structure in minimizing thermal shrinkage and cracks formation at high temperature is significant, as indicated by Bell and Kriven [92] and Sarazin et al. [91]. The aforementioned fire resistance can be achieved by structures with low conductivity and well-connected pores, reducing the pore pressure both during heating and water release by evaporation, as well as during extinguishing/cooling the heated structure to high temperatures (e.g. 1100 °C). Assuming that the greater the open porosity and gas permeability, the lower the material's ability to degrade under the pore pressure caused by moisture migration and temperature difference, materials with the greatest open porosity and moisture absorption were proposed (T100SDS, T60SDS). When the water in the porous structure is heated to a high temperature, a highly endothermic process occurs, increasing the material's fire resistance [93]. As a result of this reaction, gaseous water (water vapour) is created, which is then transferred through the porous structure to colder regions where it condenses. The situation described above illustrates the combined influence of hygrothermal performance and pore structure on fire resistance.

Furthermore, geopolymer-based foams have the potential to be employed as acoustic barriers. Several studies were focused on the acoustic characteristics of direct-foamed alkali-activated materials [94–98]. Peceño et al. [99] stated that the materials with larger total porosity absorb sound better because the sound penetrates their matrixes and dissipates the sound energy. Moreover, open pores generate continuous pathways between the interior and outside of the material matrix, resulting in enhanced permeability and good sound-absorption capacity.

Hence, two composites with the highest total porosity and open-pore volume are additionally proposed for sound absorption application. Each of these solutions aims to demonstrate how we may direct porosity to the needs of the application by utilizing a well-determined mix of surfactants based on a similarly constituted geopolymer matrix.

However, more research on the subject is required to ascertain the materials' viability for the suggested purposes.

5. Conclusions

This paper aims to propose an economical method of developing porous geopolymer with a tailored pore structure. The synergetic effect between non-ionic and ionic surfactants is revealed and its influences on the porosity, pore size distribution, pore connectivity, compressive strength and potential thermal insulation are discussed. The amount of utilized surfactants in this research is greatly decreased in this research while maintaining a similar porosity compared to existing literature. This study demonstrates that a combination of non-ionic with ionic is an effective technique in the design of foamed materials. The following detailed conclusions are resulted from this study:

1. The interactions of ionic surfactants with particles improve the stability of air bubbles. Because of the negative charge of the ash particle surface in the alkaline environment, stronger surfactant-solid particle attractions are seen for the cationic surfactant, as evidenced by a higher proportion of closed pores and lack of air voids above 500 μm. These interactions are diminished by the incorporation of nonionic surfactants, and the electrostatic repulsion between heads groups is reduced, increasing the potential of open porosity development and rising ionic surfactant molecules availability to stabilize air bubbles.
2. In comparison to ionic surfactants, lowering the CMC of the combined solution results in more densely packed bubbles. It helps to create pore cavities by decreasing the distance between bubbles. In addition, lowering CMC causes composites to have a high porosity (70 vol%), which enhances thermal insulation but diminishes mechanical performance.
3. Cationic-contained systems favour small pores formation, whereas anionic systems supply the majority of pores larger than 200 μm. A majority of voids between 50 and 200 μm, as well as a larger proportion of pores between 5 and 50 μm, are found in both cationic-based systems, independent of the kind of nonionic surfactant used.
4. The geopolymer is superior at controlling the moisture content inside the material compared to commercial reference gypsum plaster. Thanks to its greater moisture storage function at lower relative humidity, the geopolymer has a stronger humidity buffering ability to moderate changes in relative humidity of surrounding air. The variation in its effective thermal transmittance throughout the year is reduced by regulating its moisture content. The composite with the largest proportion of closed porosity (nonionic + cationic) shows the best thermal insulating performance.

Declaration of competing interest

The authors declare that they have no known competing financial interests or personal relationships that could have appeared to influence the work reported in this paper.

Table 9
Summary of pore morphology and possible application of geopolymer foams.

	T100SDS	T100CTAB	T60SDS	T60CTAB
Pore morphology	Highly-porous Majority of pores between 200 and 500 μm Open-pore structure	Highly-porous Pores above 500 μm not observed Low connectivity	Highly-porous High content of pores below 5 μm Open-pore structure Open porosity-strength balance	Low total pore volume High content of pores below 5 μm System of closed pores
Potential application	High-temperature Fire-protection Acoustic insulation	Thermal insulation	High-temperature Fire-protection Acoustic insulation	N/A

Data availability

Data will be made available on request.

Acknowledgements

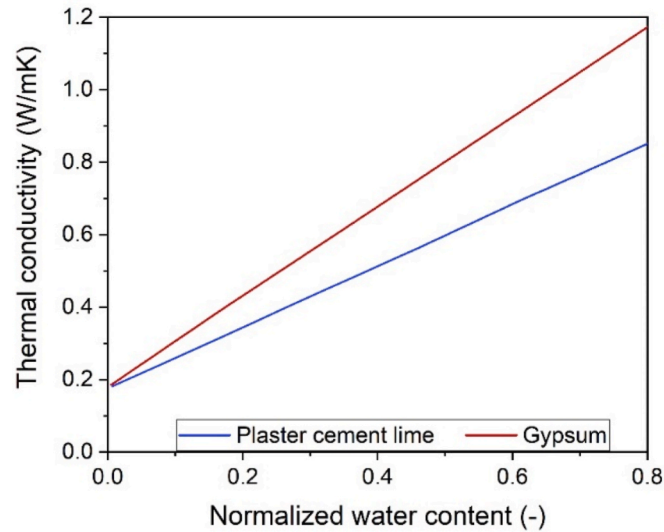This research was carried out under project number S17013a in the

Appendix

Fig. A. Moisture dependent thermal conductivity – input data for calculation.

Table A
Material properties used in time-dependent calculations (source: WUFI database)

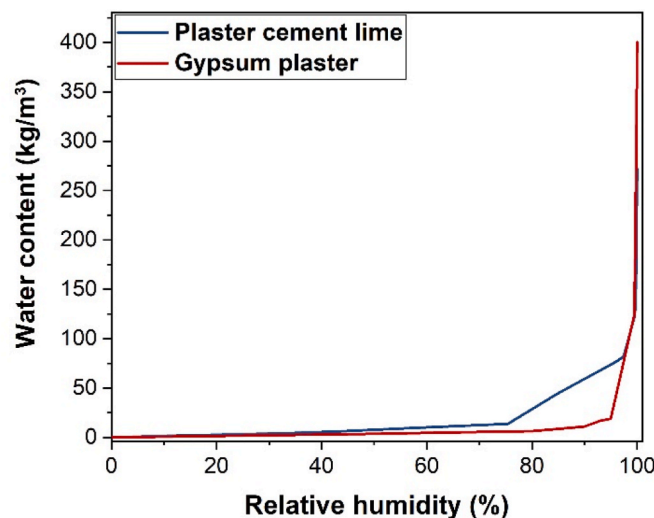|	Plaster cement lime	Gypsum
Bulk density (kg/m^3)	1024	850
Porosity (%)	61	65
Specific heat capacity (J/kgK)	850	850
Thermal conductivity (W/mK)	0.179	0.2
Water Vapour Diffusion Resistance Factor ($-$)	6.1	8.3

Fig. B. Moisture storage function of two commercially-available materials
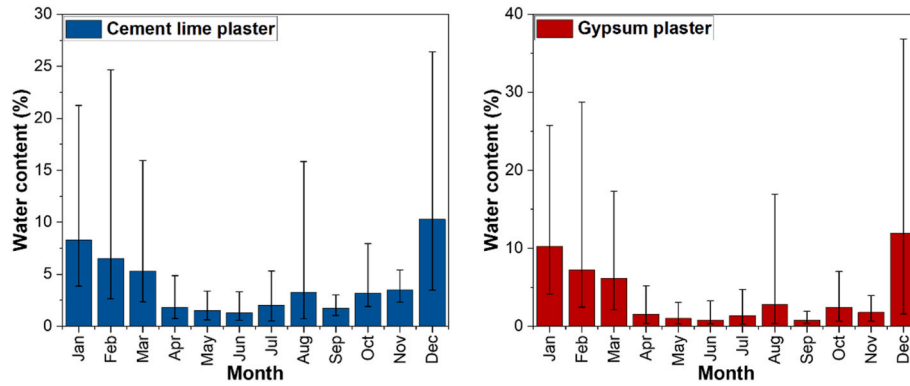
Fig. C. Moisture content of two commercial materials in the 5th year under one climate condition. With marked min and max values of water content reported in each month
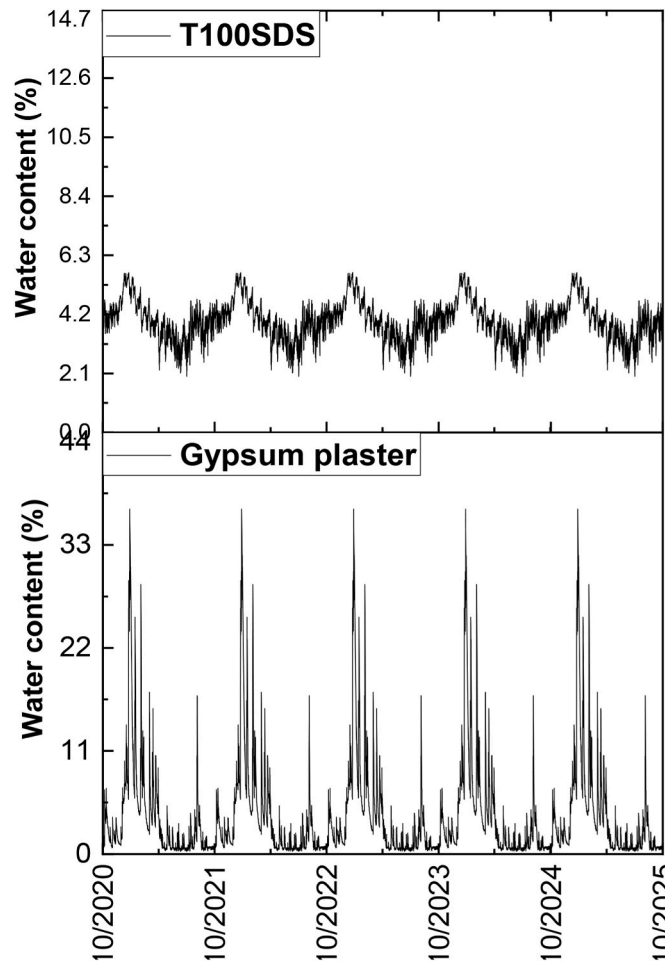

Fig. D. An example of water content in geopolymer and gypsum plaster 4 cm layers within 5 years.

References

[1] C. Bai, G. Franchin, H. Elsayed, A. Zaggia, L. Conte, H. Li, P. Colombo, High-porosity geopolymer foams with tailored porosity for thermal insulation and wastewater treatment, J. Mater. Res. 32 (2017) 3251–3259, https://doi.org/10.1557/jmr.2017.127.

[2] K.M. Klima, K. Schollbach, H.J.H. Brouwers, Q. Yu, Thermal and fire resistance of Class F fly ash based geopolymers–A review, Construct. Build. Mater. 323 (2022), 126529.

[3] L. Cao, Q. Fu, Y. Si, B. Ding, J. Yu, Porous materials for sound absorption, Compos. Commun. 10 (2018) 25–35.

[4] G. Masi, W.D.A. Rickard, L. Vickers, M.C. Bignozzi, A. Van Riessen, A comparison between different foaming methods for the synthesis of light weight geopolymers, Ceram. Int. 40 (2014) 13891–13902, https://doi.org/10.1016/j.ceramint.2014.05.108.

[5] P. Hlaváček, V. Šmilauer, F. Škvára, L. Kopecký, R. Šulc, Inorganic foams made from alkali-activated fly ash: mechanical, chemical and physical properties, J. Eur. Ceram. Soc. 35 (2015) 703–709, https://doi.org/10.1016/j.jeurceramsoc.2014.08.024.

[6] A. Hajimohammadi, T. Ngo, P. Mendis, A. Kashani, J.S.J. van Deventer, Alkali activated slag foams: the effect of the alkali reaction on foam characteristics, J. Clean. Prod. 147 (2017) 330–339.

[7] M. Strozi Cilla, M. Raymundo Morelli, P. Colombo, Effect of process parameters on the physical properties of porous geopolymers obtained by gelcasting, Ceram. Int. 40 (2014) 13585–13590, https://doi.org/10.1016/j.ceramint.2014.05.074.

[8] A. Tarameshloo, E.N. Kani, A. Allahverdi, Performance evaluation of foaming agents in cellular concrete based on foamed alkali-activated slag, Can. J. Civ. Eng. 44 (2017) 893–898.

[9] C. Bai, P. Colombo, High-porosity geopolymer membrane supports by peroxide route with the addition of egg white as surfactant, Ceram. Int. 43 (2017) 2267–2273.

[10] L. Verdolotti, B. Liguori, I. Capasso, A. Errico, D. Caputo, M. Lavorgna, S. Iannace, Synergistic effect of vegetable protein and silicon addition on geopolymeric foams properties, J. Mater. Sci. 50 (2015) 2459–2466.

[11] P. Hlaváček, V. Šmilauer, F. Škvára, L. Kopecký, R. Šulc, Inorganic foams made from alkali-activated fly ash: mechanical, chemical and physical properties, J. Eur. Ceram. Soc. (2015), https://doi.org/10.1016/j.jeurceramsoc.2014.08.024.

[12] N.A. Jaya, L. Yun-Ming, H. Cheng-Yong, M.M.A.B. Abdullah, K. Hussin, Correlation between pore structure, compressive strength and thermal conductivity of porous metakaolin geopolymer, Construct. Build. Mater. 247 (2020), https://doi.org/10.1016/j.conbuildmat.2020.118641.

[13] L. Korat, V. Ducman, The influence of the stabilizing agent SDS on porosity development in alkali-activated fly-ash based foams, Cem. Concr. Compos. 80 (2017) 168–174, https://doi.org/10.1016/j.cemconcomp.2017.03.010.

[14] S. Petlitckaia, A. Poulesquen, Design of lightweight metakaolin based geopolymer foamed with hydrogen peroxide, Ceram. Int. (2018) 1–9, https://doi.org/10.1016/j.ceramint.2018.10.021.

[15] A. Bera, K. Ojha, A. Mandal, Synergistic effect of mixed surfactant systems on foam behavior and surface tension, J. Surfactants Deterg. (2013), https://doi.org/10.1007/s11743-012-1422-4.

[16] K. Osei-Bonsu, N. Shokri, P. Grassia, Foam stability in the presence and absence of hydrocarbons: from bubble-to bulk-scale, Colloids Surfaces A Physicochem. Eng. Asp. 481 (2015) 514–526.

[17] B. Qin, Y. Lu, F. Li, Y. Jia, C. Zhu, Q. Shi, Preparation and stability of inorganic solidified foam for preventing coal fires, Adv. Mater. Sci. Eng. 2014 (2014), https://doi.org/10.1155/2014/347386.

[18] M. Wang, H. Du, A. Guo, R. Hao, Z. Hou, Microstructure control in ceramic foams via mixed cationic/anionic surfactant, Mater. Lett. 88 (2012) 97–100, https://doi.org/10.1016/j.matlet.2012.08.028.

[19] O. Owoyomi, I. Jide, M.S. Akanni, O.O. Soriyan, M.K. Morakinyo, Interactions between sodium dodecylsulphate and Triton X-100: molecular properties and kinetics investigation, J. Appl. Sci. 5 (2005) 729–734.

[20] T. Sidim, M. Arda, Some surface properties of polysorbates and cetyl trimethyl ammonium bromine mixed systems, J. Surfactants Deterg. 14 (2011) 409–414.

[21] H. Kesarwani, A. Saxena, A. Mandal, S. Sharma, Anionic/nonionic surfactant mixture for enhanced oil recovery through the investigation of adsorption, interfacial, rheological, and rock wetting characteristics, Energy Fuel. 35 (2021) 3065–3078.

[22] A. Bhatt, S. Priyadarshini, A.A. Mohanakrishnan, A. Abri, M. Sattler, S. Techapaphawit, Physical, chemical and geotechnical properties of coal fly ash: a global review, Case Stud. Constr. Mater. 11 (2019), e00263.

[23] H. Huang, Q. Yuan, D. Deng, J. Peng, Y. Huang, Effects of chemical and mineral admixtures on the foam indexes of cement-based materials, Case Stud. Constr. Mater. (2019), https://doi.org/10.1016/j.cscm.2019.e00232.

[24] K.H. Pedersen, S.I. Andersen, A.D. Jensen, K. Dam-Johansen, Replacement of the foam index test with surface tension measurements, Cement Concr. Res. (2007), https://doi.org/10.1016/j.cemconres.2007.02.007.

[25] J.G. Parra, P. Iza, H. Dominguez, E. Schott, X. Zarate, Effect of Triton X-100 surfactant on the interfacial activity of ionic surfactants SDS, CTAB and SDBS at the air/water interface: a study using molecular dynamic simulations, Colloids Surfaces A Physicochem. Eng. Asp. 603 (2020), 125284.

[26] D.M. Ćirin, M.M. Poša, V.S. Krstonošić, M.L. Milanović, Conductometric study of sodium dodecyl sulfate-nonionic surfactant (Triton X-100, Tween 20, Tween 60, Tween 80 or Tween 85) mixed micelles in aqueous solution, Hem. Ind. 66 (2012) 21–28.

[27] J. Saien, S. Asadabadi, Synergistic adsorption of Triton X-100 and CTAB surfactants at the toluene+ water interface, Fluid Phase Equil. 307 (2011) 16–23.

[28] H.J.Y. El-Aila, Interaction of nonionic surfactant Triton-X-100 with ionic surfactants, J. Dispersion Sci. Technol. 30 (2009) 1277–1280.

[29] A.H. Saiyad, A.K. Rakshit, S.G.T. Bhat, Solution and Foaming Properties of Mixed Aqueous Solution of CTAB-Triton X-100, 1995.

[30] K.R. Lange, Surfactants: a Practical Handbook, 1999.

[31] European Committee for standardization, NEN-EN 196-3 Methods of Testing Cement - Part 3: Determination of Setting Times and Soundness, 2009.

[32] E.N. Landis, D.J. Corr, Three dimensional analysis of air void systems in concrete, in: Meas. Monit. Model. Concr. Prop., Springer, 2006, pp. 517–524.

[33] L. Korat, V. Ducman, A. Legat, B. Mirtič, Characterisation of the pore-forming process in lightweight aggregate based on silica sludge by means of X-ray micro-tomography (micro-CT) and mercury intrusion porosimetry (MIP), Ceram. Int. 39 (2013) 6997–7005.

[34] Iso/Wd 12571. 2013, Hygrothermal Performance of Building Materials and Products — Determination of Hygroscopic Sorption Properties, 2010, pp. 1–22.

[35] B.S. Bsi, EN 196-1: 2005: Methods of Testing Cement, Determination of strength, 2005.

[36] K.U. Ambikakumari Sanalkumar, M. Lahoti, E.-H. Yang, Investigating the potential reactivity of fly ash for geopolymerization, Construct. Build. Mater. 225 (2019) 283–291, https://doi.org/10.1016/j.conbuildmat.2019.07.140.

[37] S.K. Nath, S. Mukherjee, S. Maitra, S. Kumar, Kinetics study of geopolymerization of fly ash using isothermal conduction calorimetry, J. Therm. Anal. Calorim. 127 (2017) 1953–1961.

[38] M. Mazur, T. Janda, W. Żukowski, Chemical and thermal methods for removing ammonia from fly ashes, Czas. Tech. (2017) 31–50, 2017.

[39] S.C. Kothekar, A.M. Ware, J.T. Waghmare, S.A. Momin, Comparative analysis of the properties of tween-20, tween-60, tween-80, arlacel-60, and arlacel-80, J. Dispersion Sci. Technol. 28 (2007) 477–484, https://doi.org/10.1080/01932690601108045.

[40] M.H. Amaral, J. das Neves, Â.Z. Oliveira, M.F. Bahia, Foamability of detergent solutions prepared with different types of surfactants and waters, J. Surfactants Deterg. 11 (2008) 275–278.

[41] L. Korat, V. Ducman, The influence of the stabilizing agent SDS on porosity development in alkali-activated fly-ash based foams, Cem. Concr. Compos. (2017), https://doi.org/10.1016/j.cemconcomp.2017.03.010.

[42] F. Xu, G. Gu, W. Zhang, H. Wang, X. Huang, J. Zhu, Pore structure analysis and properties evaluations of fly ash-based geopolymer foams by chemical foaming method, Ceram. Int. 44 (2018) 19989–19997.

[43] S. Yan, F. Zhang, J. Liu, B. Ren, P. He, D. Jia, J. Yang, Green synthesis of high porosity waste gangue microsphere/geopolymer composite foams via hydrogen peroxide modification, J. Clean. Prod. 227 (2019) 483–494.

[44] V. Cantarel, D. Lambertin, A. Poulesquen, F. Leroux, G. Renaudin, F. Frizon, Geopolymer assembly by emulsion templating: emulsion stability and hardening mechanisms, Ceram. Int. 44 (2018) 10558–10568.

[45] Y. Lu, B. Qin, Experimental investigation of closed porosity of inorganic solidified foam designed to prevent coal fires, Adv. Mater. Sci. Eng. (2015), 724548, https://doi.org/10.1155/2015/724548, 2015.

[46] J. Seuba, S. Deville, C. Guizard, A.J. Stevenson, Gas permeability of ice-templated, unidirectional porous ceramics, Sci. Technol. Adv. Mater. 17 (2016) 313–323.

[47] C. Bai, J. Zheng, G.A. Rizzi, P. Colombo, Low-temperature fabrication of SiC/geopolymer cellular composites, Compos. B Eng. 137 (2018) 23–30.

[48] M.S. Cilla, P. Colombo, M.R. Morelli, Geopolymer foams by gelcasting, Ceram. Int. 40 (2014) 5723–5730.

[49] J. Fiset, M. Cellier, P.Y. Vuillaume, Macroporous geopolymers designed for facile polymers post-infusion, Cem. Concr. Compos. 110 (2020), 103591.

[50] R. Li, G. Wu, L. Jiang, D. Sun, Characterization of multi-scale porous structure of fly ash/phosphate geopolymer hollow sphere structures: from submillimeter to nano-scale, Micron 68 (2015) 54–58.

[51] C. Bai, T. Ni, Q. Wang, H. Li, P. Colombo, Porosity, mechanical and insulating properties of geopolymer foams using vegetable oil as the stabilizing agent, J. Eur. Ceram. Soc. 38 (2018) 799–805.

[52] D.S. Smith, A. Alzina, J. Bourret, B. Nait-Ali, F. Pennec, N. Tessier-Doyen, K. Otsu, H. Matsubara, P. Elser, U.T. Gonzenbach, Thermal conductivity of porous materials, J. Mater. Res. 28 (2013) 2260–2272.

[53] S. Diamond, Mercury porosimetry: an inappropriate method for the measurement of pore size distributions in cement-based materials, Cement Concr. Res. 30 (2000) 1517–1525.

[54] S. Mindess, J.F. Young, Concrete, Prentice Hall, 2002.

[55] J. Delgado, N.M.M. Ramos, E. Barreira, V.P. De Freitas, A Critical Review of Hygrothermal Models Used in Porous Building Materials, J. Porous Media, 2010, p. 13.

[56] D. Benavente, C. Pla, Effect of pore structure and moisture content on gas diffusion and permeability in porous building stones, Mater. Struct. 51 (2018) 1–14.

[57] H. Schmidt, D. Marcinkowska, M. Cieślak, Testing Water Vapour Permeability through Porous Membranes, Fibres Text. East. Eur., 2005, pp. 66–68.

[58] T. Kato, K. Ohashi, M. Fuji, M. Takahashi, Water absorption and retention of porous ceramics fabricated by waste resources, J. Ceram. Soc. Japan 116 (2008) 212–215.

[59] Z. Jiang, Y. Xi, X. Gu, Q. Huang, W. Zhang, Modelling of water vapour sorption hysteresis of cement-based materials based on pore size distribution, Cement Concr. Res. 115 (2019) 8–19.

[60] A. Koponen, M. Kataja, J. Timonen, Permeability and effective porosity of porous media, Phys. Rev. E. 56 (1997) 3319.

[61] Z. Ji, M. Li, L. Su, Y. Pei, Porosity, mechanical strength and structure of waste-based geopolymer foams by different stabilizing agents, Construct. Build. Mater. 258 (2020) 119555.

[62] M. Masihi, R. Shams, P.R. King, Pore level characterization of Micro-CT images using percolation theory, J. Pet. Sci. Eng. 211 (2022), 110113.

[63] J. Skibinski, K. Cwieka, S.H. Ibrahim, T. Wejrzanowski, Influence of pore size variation on thermal conductivity of open-porous foams, Materials 12 (2019), https://doi.org/10.3390/ma12122017.

[64] H. Janssen, W. Van De Walle, The impact of pore structure parameters on the thermal conductivity of porous building blocks, Construct. Build. Mater. 324 (2022), 126681.

[65] G. Chen, F. Li, P. Jing, J. Geng, Z. Si, Effect of pore structure on thermal conductivity and mechanical properties of autoclaved aerated concrete, Materials 14 (2021) 339.

[66] R.M. Novais, R.C. Pullar, J.A. Labrincha, Geopolymer foams: an overview of recent advancements, Prog. Mater. Sci. 109 (2020), 100621.

[67] E. Ryshkewitch, Compression strength of porous sintered alumina and zirconia, J. Am. Ceram. Soc. 36 (1953) 65–68, https://doi.org/10.1111/j.1151-2916.1953.tb12837.x.

[68] Z. Zhang, H. Wang, The pore characteristics of geopolymer foam concrete and their impact on the compressive strength and modulus, Front. Mater. 3 (2016) 38.

[69] K. Dhasindrakrishna, K. Pasupathy, S. Ramakrishnan, J. Sanjayan, Progress, current thinking and challenges in geopolymer foam concrete technology, Cem. Concr. Compos. 116 (2021), 103886.

[70] V. Vaou, D. Panias, Thermal insulating foamy geopolymers from perlite, Miner. Eng. (2010), https://doi.org/10.1016/j.mineng.2010.07.015.

[71] L. Dembovska, D. Bajare, V. Ducman, L. Korat, G. Bumanis, The use of different by-products in the production of lightweight alkali activated building materials, Construct. Build. Mater. 135 (2017) 315–322.

[72] H.S. Hassan, H.A. Abdel-Gawwad, S.R.V. García, I. Israde-Alcántara, Fabrication and characterization of thermally-insulating coconut ash-based geopolymer foam, Waste Manag. 80 (2018) 235–240.

[73] J. Wu, Z. Zhang, Y. Zhang, D. Li, Preparation and characterization of ultra-lightweight foamed geopolymer (UFG) based on fly ash-metakaolin blends, Construct. Build. Mater. 168 (2018) 771–779.

[74] J. Feng, R. Zhang, L. Gong, Y. Li, W. Cao, X. Cheng, Development of porous fly ash-based geopolymer with low thermal conductivity, Mater. Des. 65 (2015) 529–533, https://doi.org/10.1016/j.matdes.2014.09.024.

[75] R.M. Novais, G. Ascensão, N. Ferreira, M.P. Seabra, J.A. Labrincha, Influence of water and aluminium powder content on the properties of waste-containing geopolymer foams, Ceram. Int. 44 (2018) 6242–6249.

[76] R.M. Novais, G. Ascensão, L.H. Buruberri, L. Senff, J.A. Labrincha, Influence of blowing agent on the fresh-and hardened-state properties of lightweight geopolymers, Mater. Des. 108 (2016) 551–559.

[77] Y. Cui, D. Wang, J. Zhao, D. Li, S. Ng, Y. Rui, Effect of calcium stearate based foam stabilizer on pore characteristics and thermal conductivity of geopolymer foam material, J. Build. Eng. 20 (2018) 21–29.

[78] R.M. Novais, L.H. Buruberri, G. Ascensão, M.P. Seabra, J.A. Labrincha, Porous biomass fly ash-based geopolymers with tailored thermal conductivity, J. Clean. Prod. 119 (2016) 99–107, https://doi.org/10.1016/j.jclepro.2016.01.083.

[79] C. Bai, H. Li, E. Bernardo, P. Colombo, Waste-to-resource preparation of glass-containing foams from geopolymers, Ceram. Int. 45 (2019) 7196–7202.

[80] T.F. Tadros, Applied Surfactants: Principles and Applications, John Wiley & Sons, 2006.

[81] D. Yan, S. Ruan, S. Chen, Y. Liu, Y. Tian, H. Wang, T. Ye, Effects and mechanisms of surfactants on physical properties and microstructures of metakaolin-based geopolymer, J. Zhejiang Univ. A. 22 (2021) 130–146.

[82] M.T. Ley, K.J. Folliard, K.C. Hover, Observations of air-bubbles escaped from fresh cement paste, Cement Concr. Res. 39 (2009) 409–416.

[83] Q. Liu, Z. Chen, Y. Yang, Study of the air-entraining behavior based on the interactions between cement particles and selected cationic, anionic and nonionic surfactants, Materials 13 (2020) 3514.

[84] J.C. Mendes, T.K. Moro, A.S. Figueiredo, K.D. do Carmo Silva, G.C. Silva, G.J. B. Silva, R.A.F. Peixoto, Mechanical, rheological and morphological analysis of cement-based composites with a new LAS-based air entraining agent, Construct. Build. Mater. 145 (2017) 648–661.

[85] G. Gelardi, S. Mantellato, D. Marchon, M. Palacios, A.B. Eberhardt, R.J. Flatt, Chemistry of Chemical Admixtures, Elsevier Ltd, 2016, https://doi.org/10.1016/B978-0-08-100693-1.00009-6.

[86] J. Penfold, E. Staples, I. Tucker, R.K. Thomas, Adsorption of mixed anionic and nonionic surfactants at the hydrophilic silicon surface, Langmuir 18 (2002) 5755–5760.

[87] Z. Liu, M.K. Ghatkesar, E.J.R. Sudhölter, B. Singh, N. Kumar, Understanding the cation-dependent surfactant adsorption on clay minerals in oil recovery, Energy Fuel. 33 (2019) 12319–12329.

[88] Z. Liu, G. Zhao, M. Brewer, Q. Lv, E.J.R. Sudhölter, Comprehensive review on surfactant adsorption on mineral surfaces in chemical enhanced oil recovery, Adv. Colloid Interface Sci. 294 (2021), 102467.

[89] M. Parhizkar, M. Edirisinghe, E. Stride, The effect of surfactant type and concentration on the size and stability of microbubbles produced in a capillary embedded T-junction device, RSC Adv. 5 (2015) 10751–10762.

[90] Q. Liu, Z. Chen, Y. Yang, Effect of fly ash on the air void size distribution entrained by selected anionic, cationic and nonionic surfactants in hardened cement mortars, Cem. Concr. Compos. 124 (2021), 104253.

[91] J. Sarazin, C.A. Davy, S. Bourbigot, G. Tricot, J. Hosdez, D. Lambertin, G. Fontaine, Flame resistance of geopolymer foam coatings for the fire protection of steel, Compos. B Eng. 222 (2021), 109045.

[92] J.L. Bell, W.M. Kriven, Preparation of ceramic foams from metakaolin-based geopolymer gels, Ceram. Eng. Sci. Proc. (2009) 97–112.

[93] C.N. Ang, Y.C. Wang, The effect of water movement on specific heat of gypsum plasterboard in heat transfer analysis under natural fire exposure, Construct. Build. Mater. 18 (2004) 505–515.

[94] Z. Zhang, J.L. Provis, A. Reid, H. Wang, Mechanical, thermal insulation, thermal resistance and acoustic absorption properties of geopolymer foam concrete, Cem. Concr. Compos. 62 (2015) 97–105, https://doi.org/10.1016/j.cemconcomp.2015.03.013.

[95] Y.X. Chen, K.M. Klima, H.J.H. Brouwers, Q. Yu, Effect of silica aerogel on thermal insulation and acoustic absorption of geopolymer foam composites: the role of aerogel particle size, Compos. B Eng. 242 (2022), 110048, https://doi.org/10.1016/j.compositesb.2022.110048.

[96] E. Papa, V. Medri, D. Kpogbemabou, V. Morinière, J. Laumonier, A. Vaccari, S. Rossignol, Porosity and insulating properties of silica-fume based foams, Energy Build. 131 (2016) 223–232.

[97] X. Liu, C. Hu, L. Chu, Microstructure, compressive strength and sound insulation property of fly ash-based geopolymeric foams with silica fume as foaming agent, Materials 13 (2020) 3215.

[98] C. Leiva, Y. Luna-Galiano, C. Arenas, B. Alonso-Fariñas, C. Fernández-Pereira, A porous geopolymer based on aluminum-waste with acoustic properties, Waste Manag. 95 (2019) 504–512.

[99] B. Peceño, E.M. Perez-Soriano, J.D. Ríos, Y. Luna-Galiano, H. Cifuentes, C. Leiva Fernández, Morphological analysis of porosity and sound absorption in sustainable materials from rice husk, Build. Acoust. (2022), 1351010X221103674.